Published in final edited form as:
Nat Neurosci. 2023 February ; 26(2): 350–364. doi:10.1038/s41593-022-01219-x.

A whole-brain monosynaptic input connectome to neuron classes in mouse visual cortex

A full list of authors and affiliations appears at the end of the article.

Abstract

Identification of structural connections between neurons is a prerequisite to understanding brain function. Here we developed a pipeline to systematically map brain-wide monosynaptic input connections to genetically defined neuronal populations using an optimized rabies tracing system. We used mouse visual cortex as the exemplar system and revealed quantitative target-, layer- and cell-class-specific differences in its presynaptic connectomes. The retrograde connectivity indicates the presence of ventral and dorsal visual streams and further reveals topographically organized and continuously varying subnetworks mediated by different higher visual areas. The visual cortex hierarchy can be derived from intracortical feedforward and feedback pathways mediated by upper- and lower-layer input neurons. We also identify a new role for layer 6 neurons in mediating reciprocal interhemispheric connections. This study expands our knowledge of the visual system connectomes and demonstrates that the pipeline can be scaled up to dissect connectivity of different cell populations across the mouse brain.

Introduction

The identity and function of neurons are determined not only by the inherent molecular and physiological characteristics of individual cells, but also by the synaptic connectivity through which diverse neuronal types form circuits. Although brain-wide connectomics at single-cell resolution is currently beyond our grasp for complex nervous systems with over

---

[*]Correspondence: shenqiny@alleninstitute.org, and hongkuiz@alleninstitute.org.
[#]Current address: CNC Program, Stanford University, Palo Alto, CA, USA
[†]Current address: Cajal Neuroscience, Seattle, WA 98102, USA.

Author contributions

H.Z., J.A.H., A. Cetin, S.M. and S.Y. contributed to overall project design. A. Cetin designed and orchestrated the viral tracing technology as well as viral production capability and established these with help from S.Y., T.Z. and M.T.M. S.Y., T.Z. and M.T.M. performed virus production. A. Cetin, S.Y., T.L.D. and B.O. conducted initial proof-of-principle studies. A.W. and P.A.G. supervised surgical procedures with contributions from B.O., C.N., K.M., S.L, A. Cho, L.C., K.N., N.H., E.G., J.L., R.A, R.H., and J.S. P.A.G. supervised ISI procedures with contributions from S.C., S.S., E.K.L., F.G., and T.N. M. McGraw. supervised histological processing with contributions from T.E., J.B., M. Maxwell., H.G., A.G., K.B., and A.R. P.R.N. coordinated imaging procedures with contributions from R.E., M.G., S.R., L.P., N.I.D., N.K.N. and M.J.T. L.N., L.K. and W.W. performed informatics data processing. K.E.H. and S.Y. coordinated workflow and carried out quality control. M.N. contributed to the development of data visualization tools. Q.W., S.M., J.A.H., A. Cetin, S.Y. and H.Z. formulated data generation and analysis strategies. S.Y., A. Cetin, J.A.H., B.T. and H.Z. supervised the project. S.Y. analyzed data and prepared figures. S.Y. and H.Z. wrote the manuscript with inputs from all authors.

Competing Interests

J.A.H., K.E.H., P.R.N. and K.N. are currently employed by Cajal Neuroscience. The remaining authors declare no competing interests.

Code Availability

The Allen Mouse Brain Common Coordinate Framework version 3 (CCFv3) ontology (http://atlas.brain-map.org/) was used to define brain regions. The R software (R version 3.6.0) was used for statistical tests and generation of graphs. Hierarchical clustering was conducted using the pvclust package (pvclust_2.2-0) in R (R version 3.6.0). Numbers of starter cells in confocal images were quantified using the Cell Counter plugin in ImageJ (ImageJ 2.0.0-rc-43/1.53j).

millions of neurons, different strategies have been applied to reveal the connectivity at distinct levels of resolution, including anterograde and retrograde tracing, brain-wide full morphology reconstruction, multiple-patch clamp recording, optogenetics-assisted circuit mapping, and electron microscopy.

Systematic mapping of afferent connectivity to specific cell populations has been greatly aided by the introduction of the monosynaptic, retrograde trans-synaptic rabies virus system[1,2]. Rabies glycoprotein (RG)-deleted rabies viruses can be coupled with various genetic and viral tools to ensure cell-type specific labeling of direct presynaptic inputs[3–15]. Many efforts have been made to improve the efficiency and specificity of rabies virus tracer while reducing its toxicity, including the construction of recombinant rabies viruses from the CVS N2c virus strain[16], utilization of an engineered RG[4], and generation of a double-deletion-mutant rabies virus[17] and a self-inactivating rabies virus[18]. In addition, an intersectional rabies tracing strategy targeting Flp- and Cre-double labeled neurons has been generated to conduct cell-type-specific circuit tracing with greater accuracy[19].

In our effort to build the Allen Mouse Brain Connectivity Atlas, we combined viral tools, transgenic mouse lines, high-throughput imaging, and informatics to map brain-wide efferent connections at the level of cell classes[20,21]. By delivering recombinant adeno-associated viruses (AAV) with Cre-dependent expression of EGFP to target brain areas of Cre transgenic lines, we labeled axons from selective Cre$^+$ neuronal classes and subclasses. Our informatics pipeline, which includes registration of image series to the Allen Mouse Brain Common Coordinate Framework (CCF) and automatic segmentation of fluorescent axonal projections[22,23], enabled quantification and comparison of whole-brain projections across multiple regions and cell classes. The resulting high-resolution mesoscale projection maps provide the foundation for in-depth dissection of the logic of mouse brain connectivity.

Aiming to construct a complementary afferent map of mouse brain-wide connectivity, we developed an improved version of the monosynaptic rabies virus tracing system and incorporated rabies-mediated presynaptic input mapping into our pipeline. Our system consists of a single AAV helper virus that allows the accurate identification of starter neurons and a rabies virus expressing nucleus-localized EGFP marker to facilitate automatic quantification of presynaptic inputs. In this study, we utilized this pipeline to map brain-wide, cell-class-specific, presynaptic connectomes for the mouse visual cortex, including both primary and higher visual areas. Mouse visual cortex contains at least ten visuotopically organized cortical areas[24–27]. These visual areas are strongly interconnected to form a hierarchical network with two visual streams as revealed by anterograde tracing[20,28], similar to what have been known in primates and cats[29]. In primates, visual cortical hierarchy was defined by feedforward and feedback connections via laminar distribution of retrogradely labeled neurons[30]. It remains largely unknown whether visual hierarchy and streams in mouse can also be defined with retrograde tracing.

By applying the monosynaptic rabies tracing system to Cre driver mouse lines labeling different glutamatergic excitatory and GABAergic inhibitory neuron subclasses[20,31], our results reveal quantitative target-, layer- and cell-class-specific differences in the retrograde connectomes. We find that the retrograde connectomes of the same cell classes in different target areas are more different from each other than the retrograde connectomes of different cell classes in the same target area. Layer (L)-specific features are also identified, for example, L4 neurons receive more thalamic inputs and fewer inputs from higher-order association cortical areas, whereas L6 neurons are the main targets of contralateral/callosal inputs. Our study confirms previous findings of the dorsal and ventral streams in the mouse visual cortex[28] and further reveals distinct subnetworks in the medial and lateral parts of the dorsal stream as well as several transitional areas between the streams or subnetworks. Finally, our previous study showed that the hierarchical organization among different areas of the mouse visual cortex can be derived from axon termination patterns in the anterograde connectomes[20], here we demonstrate that it can also be derived from the retrograde connectomes independently, via the feedforward and feedback projections mediated by upper- and lower-layer input neurons, respectively.

Results

A pipeline for the mesoscale retrograde connectome

To systematically map whole-brain presynaptic inputs to different cell classes, we established a standardized pipeline based on our pipeline for projection mapping across the entire brain[20,21] (Figure 1). The monosynaptic cell-type-specific rabies tracing system consists of EnvA-pseudotyped and glycoprotein-deleted rabies virus (EnvA RV^{dG}, in CVS N2c strain) expressing histone-tagged EGFP (H2B-EGFP) and AAV helper virus conditionally expressing the red fluorescent protein dTomato, the EnvA receptor (TVA), and the rabies glycoprotein (RG). This system was coupled with Cre-driver mouse lines to reveal inputs to defined cell classes or types.

We re-engineered several features of pre-existing rabies tracing tools[10,16,32] to facilitate accurate identification of starter cells and automatic quantification of presynaptic inputs (Figure 1a). Our AAV helper virus used the FLEX strategy to conditionally express a tricistronic cassette of TVA^{66T}-P2A-dTomato-P2A-RG under the control of human synapsin promoter (hSyn), and the ATG of the tricistronic cassette was placed 5’ to the FLEX sites[32] (Figure 1a). The co-expression of TVA, dTomato, and RG from the same expression cassette allows unambiguous identification of starter neurons[33]. This single AAV helper, with the use of the attenuated form of TVA, TVA^{66T}, significantly reduced spurious virus labeling in the absence of Cre (Extended Data Figure 1a–c, Supplementary Table 1). Our rabies tracer is based on the CVS $N2c^{dG}$ rabies strain[16] and expresses H2B-EGFP. Compared with the EGFP-expressing and H2B-EGFP-expressing SAD $B19^{dG}$ rabies viruses (Extended Data Figure 1d–f, Supplementary Table 1), the H2B-EGFP-expressing CVS $N2c^{dG}$ virus mediates stringent nucleus labeling, which facilitates automatic quantification of presynaptic cells by minimizing neurite labeling. This is the virus that we have used throughout the paper and will refer to simply as RV-H2B-EGFP.

We performed several control experiments to verify the specificity of the rabies virus tracing system in the absence of Cre, in the absence of RG provided by AAV helper virus, or in transgenic lines in which Cre is expressed in non-neuronal cell types (Extended Data Figure 2, Supplementary Table 1). The results confirm that the presynaptic labeling is specific for the Cre^+ neuronal starter cells expressing the tricistronic cassette and infected with the RV-H2B-GFP rabies virus. Our rabies tracing strategy presents minimal non-specific labeling in the absence of Cre and enables unambiguous identification of starter cells and automatic quantification of presynaptic inputs.

Cell-class-specific mapping of inputs to visual areas

We utilized our retrograde connectome pipeline to systematically map the presynaptic inputs of neurons in the visual areas by layers and cell classes. Half of all injections were guided by maps derived from ISI (271/519), while others (248/519) were conducted using atlas-derived stereotaxic coordinates (Extended Data Figure 3a). After excluding experiments showing no virus labeling, tissue damage, segmentation error, or wrong targeting, 303 experiments across ten excitatory neuron Cre lines, seven interneuron Cre lines, and one Cre line labeling both excitatory neurons and interneurons were included in the analysis (Figure 2a, Extended Data Figure 3a, Supplementary Tables 2–3). Many of these Cre lines were previously used in the Allen Mouse Connectivity Atlas to identify the organization of cortical connections in the mouse brain[20], as well as in previously published rabies studies. All but one experiment (which targeted the temporal association area, TEa) successfully targeted the visual areas (jointly labeled as VIS), including primary visual cortex (VISp, or V1), and higher visual areas (HVAs) such as lateral visual area (VISl, or LM), posteromedial visual area (VISpm, or PM), anteromedial visual area (VISam, or AM), anterior area (VISa, or A), anterolateral area (VISal, or AL), rostrolateral visual area (VISrl, or RL), laterointermediate area (VISli, or LI), postrhinal area (VISpor, or POR), and posterolateral area (VISpl, or PL). Fourteen experiments targeted a subarea of the primary somatosensory area barrel field (SSp-bfd) bordering VISrl, which corresponds to previously defined VISrll (or RLL) region and displays extension of retinotopic organization lateral to VISrl[25], and thus we refer to this barrel field subarea as SSp-bfd-rll. Locations of all injection centroids were plotted onto the CCFv3 cortical flat map (Figure 2b).

We quantified presynaptic inputs in each brain region using an automated image segmentation algorithm trained to detect the fluorescence signal from nucleus-localized H2B-EGFP[23]. We validated the accuracy of automatic signal detection and quantification of inputs following registration to the Allen CCFv3[22] by obtaining high correlation between the informatically measured per structure input signal volume (sum of detected signal in mm^3) and manual counting of labeled cells (Extended Data Figure 3b–h). Therefore, we used the automatically calculated input signal volume of each structure for subsequent analysis.

We find that dTomato-labeled starter cells show distinct layer-specific distribution patterns consistent with the Cre expression. The numbers of starter neurons vary between Cre lines and between different experiments within the same Cre line (Extended Data Figure 3i–j, Supplementary Table 2). Although the overall presynaptic labeling signal increases with the number of starter cells, there is not a strong linear correlation ($R^2 = 0.54$) between the number of starter cells and total input signal volume within the brain (Extended Data Figure 3k). It suggests that postsynaptic cells may receive convergent inputs from presynaptic cells, which in turn can make divergent connections to different postsynaptic cells. Previously, we compared whole-brain projections across animals by normalizing the projection signals to the size of the infection area[20]. Here, due to the lack of strong linear correlation between whole brain input signal and the number of starter cells in the injection site, we instead use the fraction of whole brain inputs as our measure of connectivity strength per region, i.e., the input signal volume per brain structure divided by the total input signal volume of the entire brain.

We next constructed a brain-wide matrix for inputs to the visual areas, focusing on the fraction of whole brain inputs from 314 anatomical structures at a mid-ontology level from the CCFv3 (Figure 2c, Supplementary Table 3). Hierarchical clustering analysis of the inputs from the 314 brain regions shows separation of all 303 experiments into three major clusters that are correlated with the spatial proximity of the injection sites: the VISp and posterior and lateral HVA cluster (VISpor, VISpl, VISl and VISal), the anterolateral cluster (SSp-bfd-rll, and VISrl), and the anteromedial cluster (VISam, VISpm, and VISa). Compared to the brain-wide output projections from mouse visual areas[20], presynaptic inputs come from a broader collection of brain regions (Figure 2c). Visual areas receive the strongest inputs from isocortex, followed by thalamus and hippocampal formation (HPF) (Extended Data Figure 3l). Fifteen cortical areas account for the majority of isocortical inputs excluding the visual and medial modules where the injection targets locate, and nine thalamic nuclei account for the majority of thalamic inputs (Extended Data Figure 3m–n).

Brain-wide inputs to VISp and HVAs

We compared presynaptic inputs across all experiments in VISpor, VISli, VISp, VISl, VISal, VISrl, VISa, VISpm, VISam and SSp-bfd-rll. Comparison of bilateral inputs from the isocortical modules[20] and the rest of the brain to these ten target areas reveals overall similar, but quantitatively different global input patterns to different targets, with dominant inputs from the isocortical modules and thalamus (Figure 3a). Visual areas also receive strong presynaptic inputs from HPF, which are mainly found in lateral entorhinal cortex (ENTl), medial entorhinal cortex (ENTm), CA1 and the post-, pre- and parasubiculum (POST, PRE, and PAR) (Extended Data Figure 4).

Inputs from other anatomical structures each provide less than 1% of whole brain inputs, and the fractions of inputs span more than three orders of magnitude (Extended Data Figure 4, Supplementary Table 3). The distribution of subcortical inputs strongly suggests the involvement of neuromodulatory systems in regulating visual cortical function. Clustered inputs are found in NDB and substantia innominata (SI), consistent with the innervation of visual cortex by basal forebrain cholinergic neurons[34,35]. Our results reveal sparse locus coeruleus (LC) inputs to both VISp and HVAs, suggesting that visual cortex is part of the ascending noradrenergic efferent pathway innervating the limbic system, midbrain, thalamus, basal forebrain and neocortex[36,37]. In dorsal raphe (DR) where dorsal cortex-projecting serotonin neurons were previously identified[38], sparsely labeled presynaptic neurons are also found. Identification of monosynaptic projections from neuromodulatory neurons to both VISp and HVAs suggests that locally released neuromodulators can affect all levels of visual information processing.

We then focused on individual cortical and thalamic source regions that send most inputs to visual target areas (Extended Data Figure 3m–n) and used the average from all experiments (including all Cre lines) in the same target to compare the input strength from a given presynaptic region to the ten visual targets (Figure 3b–d). The input patterns strongly support the presence of two subnetworks equivalent to the dorsal and ventral cortical streams. The nodes in the dorsal and ventral streams of the mouse visual system were adopted from previous studies based on the anterograde projection strength, with VISl, VISli, VISpl and VISpor in the ventral stream, and VISal, VISrl, VISa, VISam and VISpm in the dorsal stream[28]. We find that dorsal stream areas tend to receive higher proportions of inputs from each other and lower proportions of inputs from ventral stream areas, whereas ventral stream areas receive notable inputs from areas in both streams (Figure 3b–c). We also place SSp-bfd-rll as part of the dorsal stream, because it shows similar input pattern characteristic of dorsal stream structures as its adjacent area VISrl. VISp in general has similar input pattern as the ventral stream node, VISl. However, VISp can be distinguished from VISl and other HVAs based on the preference for inputs from the dorsal lateral geniculate complex (LGd) of thalamus over the lateral posterior nucleus (LP) of thalamus (Figure 3d).

Within the dorsal stream, anterolateral areas such as VISal, VISrl and SSp-bfd-rll present strong inputs among themselves, while receiving relatively few inputs from the medial areas such as VISam and VISpm (Figure 3b–c). In contrast, VISam and VISpm show strong mutual connections, while VISpm receives relatively few inputs from the anterolateral areas (Figure 3b–c). In addition, the anterolateral areas receive higher proportions of inputs from the somatomotor module, whereas the medial areas VISam and VISpm receive higher proportions of inputs from RSP, ACA and ventrolateral orbital area (ORBvl) (Figure 3b–c). The anterolateral and medial areas also have distinct thalamic input patterns, with VISam and VISpm receiving strong inputs from anteromedial nucleus (AM) and lateral dorsal nucleus (LD) and anterolateral areas receiving strong inputs from posterior complex (PO) and ventral anterior-lateral complex (VAL) (Figure 3d). Such input patterns can be observed in both excitatory neuron and interneuron experiments (Extended Data Figure 5). To evaluate the similarity of input patterns between different targets, we calculated Spearman's correlation coefficients (R) for experiments within the same target and across different targets (Figure 3e). Our results suggest the possibility of two subnetworks in the dorsal stream, one consisting of medial areas of VISam and VISpm and the other consisting of anterolateral areas of VISal, VISrl, SSp-bfd-rll and VISa, with a gradual transition between the two subnetworks from medial to lateral.

Our results also suggest that VISal and VISpm may be transitional areas between dorsal and ventral streams. VISal's cortical input pattern is generally more similar to other dorsolateral HVAs, but it also receives inputs from ventral HVAs (albeit weakly) as well as lateral cortical areas (e.g., TEa and AUDp) like the ventral HVAs do (Figure 3b–c). VISpm's cortical input pattern is the most similar to VISam, but also receives more inputs from ventral HVAs (e.g., VISl) and TEa than dorsolateral HVAs and somatomotor areas (Figure 3b–c). Furthermore, VISal shows high inter-area correlations with areas in both dorsal and ventral streams, and VISpm shows high inter-area correlations only with VISam, VISl and VISp (Figure 3e). Hierarchical clustering of the input patterns for all experiments (Figure 2c) also places VISal in the posterior/ventral cluster. Together, the identification of these transitional areas between the dorsal and ventral streams and the above two subnetworks within the dorsal stream suggests that the mouse visual cortical system is more complex than a simple two-stream system.

Given the unique input pattern to each visual area, we further investigated the effects of different starter cell classes on the input patterns. We find that the correlation between input patterns of different cell classes in the same target is higher than that of the same cell class in different targets (Figure 3f). Using experiments in VISrl and VISpm as examples, regardless of the starter cell classes, VISrl receives characteristically higher proportions of inputs from ACAd, MOs, and SSp-bfd than VISpm, whereas VISpm receives higher proportions of inputs from ACAv, and RSP than VISrl (Figure 3g). The results suggest that the presynaptic input patterns, as quantified by our tracing system, are predominantly determined by the spatial location of the starter cells, and that different cell classes in the same target receive similar global input patterns.

Visual responses in the mouse VISpor have been shown to rely on the colliculo-cortical pathway and are independent of the geniculo-cortical pathway[39]. The proportions of LP inputs to VISpor were over 10 times those of LGd inputs (Figure 3h), consistent with the major relay of SC visual input through LP to VISpor. Sparse SC inputs are found in 11% of all experiments (Supplementary Table 3), and the mean proportion of SC inputs is at ~0.001% of whole brain inputs. However, two VISpor experiments using the Cux2-IRES-Cre line consistently showed inputs from SC, sensory related (SCs), up to around 0.2% of total inputs (Figure 3h–i). This result suggests a potential direct monosynaptic connection between SCs and VISpor, in addition to the disynaptic connection between SC and VISpor via LP. Better genetic tools targeting more defined cell types in VISpor are required to further dissect the identities of monosynaptic connection from SCs to VISpor.

Brain-wide inputs to excitatory neurons in different layers

We next focused on quantifying the brain-wide inputs to different Cre-defined glutamatergic excitatory neuron subclasses within a single target area, VISp. Despite the variation in starter cell numbers and layer distributions (Extended Data Figure 6a–c), the overall input patterns to VISp are similar between different Cre driver lines (Extended Data Figure 6d–e), with most inputs arising from isocortex, followed by thalamus and HPF. Compared to other layer-specific lines, the L4 line receives a significantly higher proportion of inputs from thalamus ($p < 0.001$, Tukey multiple comparisons of means), consistent with the notion that feedforward signal from the visual thalamus is mostly received by L4 neurons in the visual cortex[40–44].

We constructed an input connectivity matrix for experiments targeting 9 Cre-defined excitatory neuron populations in VISp (Figure 4a, Extended Data Figure 7a), and compared that to the brain-wide output projection matrix (Supplementary Table 4) for the same Cre-defined neuron populations in VISp (Figure 4b, Extended Data Figure 7b). VISp receives the highest proportions of inputs from areas within the visual module, followed by visual areas within the medial module. Outside these areas, VISp excitatory neurons receive the majority of inputs from ACA and ORB in the prefrontal module, TEa and ectorhinal (ECT) areas in the lateral module, SSs, SSp-bfd, and MOs in the somatomotor module, RSP in the medial module, and the auditory module.

The striking similarity between the intracortical input and output patterns of VISp reveals the reciprocity of corticocortical connections (Figure 4a–b). However, it is interesting to note that the interconnection between VISp and auditory areas (AUD) is not symmetric in strength. All VISp excitatory neuron populations receive high proportions of inputs from but send weak projections to AUD, consistent with anterograde tracing data (Experiments 554421791 and 536299435 in Allen Mouse Brain Connectivity Atlas)[20,21].

Out of the nine thalamic nuclei with the strongest inputs to VISp (Figure 4a), three nuclei, LGd, LP and LD, collectively account for more than 70% of the thalamic inputs. These three nuclei also receive strong VISp projections from L6 CT neurons labeled by Ntsr1-Cre as well as L5 ET neurons labeled by Rbp4 and A93 Cre lines (Figure 4b), with L6 CT mainly targeting LGd and L5 ET preferentially targeting LP and LD. The brain-wide monosynaptic input matrix also reveals that VISp receives strong inputs from ENTl, ENTm, PAR, POST, CLA and NDB (Extended Data Figure 7a).

We then compared the input patterns of excitatory neurons in different layers of VISp (Figure 4a,c, Extended Data Figure 7a,c). L4 neurons receive the least proportions of inputs from higher-order association cortical areas, including ACA, ORBvl, TEa and RSP, as well as from subcortical input areas, and receive a significantly higher proportion of inputs from LGd (between L4 neurons and those from other layers: $p < 0.005$, Tukey multiple comparisons of means). In contrast, L2/3, L5 and L6 neurons generally receive higher proportions of inputs from higher-order association cortical areas, and both L5 and L6 neurons receive the highest proportions of inputs from RSPv as compared to other association cortical areas[45,46]. Both RSP and ACA send the highest proportions of inputs to L6 neurons, while ORBvl sends the highest proportion of inputs to L5 neurons. These layer-specific input patterns are supported by the axon lamination patterns from cortical and thalamic areas to VISp (Figure 4d), where ORBvl axons primarily ramify in L1 and L5 of VISp, ACAd axons mainly reside in L1 and L6, RSPv axons are mainly found in L6, followed by L5 and L1, and axons from LGd mainly ramify in L4.

Subsequently, we analyzed the laminar distribution of cortical inputs to excitatory neurons in different layers (Figure 4e–k). Presynaptic input neurons in higher-order association cortical areas are often located in deep layers (L5 and L6), regardless of the layer location of starter cells in VISp. For example, in ipsilateral ACAd, L5 contains the most presynaptic neurons compared to other layers, with a similar preference for L5 observed for inputs to excitatory neurons located in different layers of VISp (Figure 4e). A notable exception is ipsilateral ORBvl, in which VISp L2/3, L4 and L5 neurons preferentially receive inputs from L2/3 ORBvl whereas no preference in layer distribution is found for input to L6 neurons of VISp (Figure 4f). We also observe interesting patterns of differential layer preference in inputs from homotypic ipsilateral and contralateral cortical areas to VISp (Figure 4g–k).

These distinct features in brain-wide input patterns to excitatory neurons in different layers of VISp can also be found in VISl (Extended Data Figure 7d–l, Supplementary Table 5). Similar to VISp, L4 of VISl overall receives higher proportions of inputs from thalamic areas and lower proportions of inputs from higher-order cortical areas, most input neurons in higher-order cortical areas reside in deep layers, and ipsilateral and contralateral cortical areas present different laminar distribution of input neurons to the same target.

Distinct presynaptic inputs to L6 excitatory neurons of visual areas

L6 CT and L6b neurons (labeled by Ntsrt1 and Ctgf Cre lines) in VISp clearly receive a higher proportion of their inputs from the contralateral cortex compared to excitatory neurons in the other layers (Figure 4a, Extended Data Figure 6d). These inputs mostly originate from the contralateral visual, medial, and auditory modules. A comparison with L5 neuron populations (labeled by Tlx3, A93-Tg1 and Rbp4 Cre lines) shows that these L6 neurons receive similarly high proportions of inputs from ipsilateral HVAs and RSP as the L5 neurons, but significantly higher proportions of contralateral inputs ($p < 0.01$, Tukey multiple comparisons of means, Figure 4l).

To further investigate whether the layer distribution of starter neurons is the key factor in determining the level of contralateral inputs, we identified 89 experiments in VISp and HVAs with starter cells restricted to a single layer and compared the contralateral and ipsilateral inputs between the experiments. Overall, L6 neurons across VIS receive a higher proportion of contralateral inputs from all six isocortical modules than neurons in other layers (Extended Data Figure 8a–c). Quantitative analysis suggests that the effect of layer on the ratio of contralateral to ipsilateral isocortical inputs is significant (two-way ANOVA, $p < 0.001$), and that the location of the target site (VISp or HVAs) does not significantly affect the ratio of contralateral to ipsilateral isocortical inputs ($p = 0.37$). As shown for the homotypic contralateral inputs to L6 neurons (Extended Data Figure 8d), presynaptic neurons mediating interhemispheric connectivity of the visual areas mainly locate in deep layers (L5 and L6). Our results suggest that L6 of the visual areas has distinct retrograde connectivity compared to the other layers.

Brain-wide inputs to VISp interneurons

To explore presynaptic inputs to distinct GABAergic interneurons, we employed various Cre lines labeling major interneuron subclasses: Pvalb-Cre, Sst-Cre, Vip-Cre and Ndnf-Cre, as well as Gad2-Cre to cover all cortical interneurons. Even though the majority of Ndnf-expressing neurogliaform cells are in L1, in our experiments starter cells in the Ndnf line were found in L2 with the exception of one experiment targeting VISl. We believe that tissue damage caused by injections disproportionally ablates L1 cells, leading to the absence of L1 starter cells in most experiments.

Despite variation in starter cell numbers (Extended Data Figures 3, 6, 9a) and layer distribution (Extended Data Figures 6, 9b), the overall global patterns are again similar between Cre lines, regardless of excitatory or inhibitory classes (Figure 5a, Extended Data Figures 6, 9c–d). Compared to excitatory neurons, interneurons in VISl, VISp and VISam overall receive a higher proportion of their inputs from thalamus and ipsilateral cortical module where the target areas locate and a lower proportion of their inputs from contralateral cortical modules (Figure 5b), suggesting that intra-module inputs exert greater influence on interneurons than excitatory neurons.

We then focused on different interneuron subclasses in VISp and find that the three interneuron subclasses, Sst, Vip and Pvalb, receive similar patterns of inputs from ipsilateral cortical and thalamic areas (Figure 5c). We divided the 39 interneuron experiments in VISp from all Cre lines into four different groups based on the depth of starter cell population: the Top group contained experiments with starter cells restricted to L2/3 (we found very few L1 starter cells), whereas the Upper, Lower, and Bottom groups had progressively more starter cells in deep layers (Figure 5d). Although starter cells in these groups are rarely restricted to a single layer, we find distinct input patterns of interneurons, especially between the Bottom group and others. The Bottom group receives a significantly lower proportion of inputs from LGd compared to the Upper and Lower groups ($p < 0.01$, independent two sample t test (two-sided)), and significantly higher proportions of inputs from ACA and RSP compared to all other groups (ACA: $p < 0.001$, RSP: $p < 0.05$, independent two sample t test (two-sided)) (Figure 5e). Consistent with the observation of L6 excitatory neurons receiving extensive contralateral cortical inputs, the Bottom group also receives higher proportions of contralateral cortical inputs than the other groups (Figure 5e). Statistically significant differences in inputs from the contralateral non-visual cortical modules were found between the Bottom group and the other three groups ($p < 0.05$, independent two sample t test (two-sided)). Interneuron subclasses with starter cells mostly outside of L6 tend to receive lower proportions of contralateral inputs than the Bottom group,, whereas Gad2 experiments with many starter cells in L6 receive comparable levels of contralateral inputs as the Bottom group (Figure 5f).

Local inputs to excitatory and inhibitory neurons

In experiments where starter cells were restricted to a specific layer of VISp or VISl, we also examined local inputs (Figure 6, Extended Data Figure 9e–h). We define the layer preference of any local inputs as the fraction of inputs in that layer compared to all local inputs. We find that starter cells in each layer have characteristic local input patterns.

For VISp excitatory neurons (Figure 6a–h), L2/3 neurons preferentially receive inputs from L4 and L5. L4 neurons receive the fewest inputs from L2/3 and preferentially receive inputs from L4 and L5. L5 neurons receive strong inputs from L2/3 to L6, with a preference for L2/3 and L5 inputs, and L6 neurons preferentially receive inputs from deeper layers. With the exception of L2/3, starter cells receive dense inputs from other cells in the same layer. Our results shown dense inputs from L4 to L2/3, despite weak inputs from L2/3 to L4, and dense reciprocal inputs between L2/3 and L5. Excitatory neurons in VISl also exhibit characteristic local input patterns similar to excitatory neurons in VISp (Extended Data Figure 9e–h).

Considering the layer-specific local input patterns observed in excitatory neurons, we compared local input patterns of interneurons among the four different groups based on the depth of starter cell distributions (Figure 6i–j). The Top group includes two Ndnf experiments and two Vip experiments, with the Ndnf starter cells receiving a higher proportion of inputs from L5, and the Vip starter cells receiving higher proportions of inputs from L4 and L5. The Upper, Lower, and Bottom groups each exhibit distinct local input patterns, with the Bottom group receiving a higher proportion of inputs from L6 than the

Upper group. Our results suggest cell-class- and layer-dependent local input patterns for both excitatory neurons and inhibitory interneurons[47,48].

Hierarchical order defined by presynaptic inputs

We explored whether the laminar distribution of presynaptic inputs among visual areas reveals the hierarchical ordering of these areas. In primates, the hierarchy of visual cortical areas was derived by designating feedforward connections originating from superficial layers in a lower area and terminating in L4 in a higher area, and feedback connections originating from deeper layers in a higher area and terminating outside L4 in a lower area[29]. Other studies used the fraction of labeled presynaptic supragranular neurons (SLN), defined as the number of labeled neurons in L2/3 divided by the sum of labeled neurons in supra- and infra-granular layers (L2/3 + L5 + L6), to derive a hierarchical ordering of the primate visual cortical areas that was consistent with the Felleman and Van Essen hierarchy[29,30]. Unlike what was described for primates, L4 neurons in mouse VISp do appear to play an important role as the other layers in information relay to HVAs. A preference for L4 inputs from VISp is particularly noticeable for VISrl and SSp-bfd-rll, with the highest fraction of VISp inputs coming from L4 (Extended Data Figure 10).

In an effort to identify a quantitative hierarchical parameter for visual cortical areas using retrogradely labeled cells, we first compared the laminar distribution of presynaptic inputs for the connections between VISp and VISam (Figure 7a), which were shown to lie at the base and the top of the visual area hierarchy previously[20]. Accordingly, inputs from VISam to VISp are considered feedback, whereas those from VISp to VISam are considered feedforward inputs. We find that the percentages of L2/3 and L4 inputs from VISp to VISam are significantly higher than those from VISam to VISp, and the percentage of L5 inputs from VISam to VISp is significantly higher than that from VISp to VISam ($p < 0.001$, two sample t-test, in both cases). In contrast, the percentage of L6 input does not differ between the two directions. Inputs from L2/3/4 and L5 of other visual areas to VISp or VISam present complementary patterns consistent with the predicted relative hierarchical positions of each source area and target area based on laminar projection patterns (Figure 7b–c). Inputs from almost all other ipsilateral cortical areas to VISp also show lower fractions of L2/3/4 inputs and higher fractions of L5 inputs than intra-VISp inputs (Figures 7d–f), consistent with the distinct roles of L2/3/4 and L5 in feedforward and feedback information relay. In contrast, the fraction of L6 inputs is not correlated with feedforward or feedback hierarchical orders (Figure 7b–c) but shows a lateral to medial gradient with higher inputs from the lateral areas and lower from the medial areas (Figure 7d–f).

Our observations suggest that the ratio of inputs from the superficial L2/3/4 to the sum of inputs from the superficial layers and L5 [i.e., (L2/3 + L4) / (L2/3 + L4 + L5), hereinafter referred to as the h index] could be used to quantify the hierarchical positions of the mouse visual areas. We calculated the average h index for presynaptic inputs from 10 source visual areas to 9 target visual areas, using both excitatory and inhibitory neuron experiments (Figure 7g). For a given target, inputs from VISp exhibit the highest h index values as compared to the HVAs, consistent with VISp at the lowest hierarchical position, and inputs from HVAs of higher hierarchical positions in the ventral and dorsal streams have lower *h* index values as compared to other HVAs in the same stream.

To explore whether *h* index can serve as a quantitative parameter for hierarchical distance between cortical areas, we performed correlation analysis of *h* values measured between common cortical source areas and paired visual targets (Figure 7h). We hypothesized that if the measured *h* index faithfully reflects the hierarchical distance between the target area and the source area, the difference between *h* values measured for a common source area and paired target areas would be the hierarchical distance between the two target areas. This relationship would be translated into a best-fit line with a slope equal to 1 and an intercept indicating the hierarchical distance between the two target areas when plotting paired *h* values measured for common cortical source areas. We compared the paired *h* values between all cortical source areas and five target visual areas, with VISpm excluded for the lack of L4 experiments and VISa excluded for low sample size. Overall, we found a fair correspondence between the best fit lines based on the least-squares criterion and the best fit with a slope equal to 1. We then fit a linear regression model to the measured *h* values between cortical source areas and the five visual areas with the hierarchical level of VISp set at zero. The relative hierarchical orders of cortical areas were estimated to best predict the measured *h* index values. A strong correlation ($R^2 = 0.94$) was found between the predicted *h* values and the measured values (Figure 7i). The estimated hierarchical levels for the visual areas (Figure 7j) are overall consistent with the predicted hierarchy based on the cell-type-specific projection[20], with the exception that the linear model fitting *h*-index values places VISa at the top of the dorsal stream instead of VISam. Consistent with our previous findings, we find that the hierarchy in the mouse visual cortex is shallow, especially for the dorsal stream.

Discussion

Here we present the construction and validation of a retrograde connectome pipeline for the mouse brain, with a focus on the visual cortical areas. With improved virus tools and informatic processing, our pipeline can be utilized to conduct large-scale systematic mapping of brain-wide presynaptic inputs at the cell class or type level. Together with our anterograde projection mapping pipeline, the current work proves the feasibility to build a comprehensive, directional, and 3D connectivity atlas of the mouse brain at the cell type level.

Target, layer and cell class co-define input connectivity

Our retrograde connectome dataset reveals that the presynaptic inputs to defined neuronal classes are determined predominantly by target area, followed by layer distribution of starter cells and Cre line-defined cell classes. In contrast to the highly differential cell-class-specific anterograde projection patterns, rabies tracings from Cre-defined cell classes in the same target reveal overall similar global input patterns (Figures 3f–g, 4a,c, Extended Data Figure 7d,f). Similar results were obtained when we applied the same approach described in this study to another mouse cortical area, the primary motor cortex[49], as well as in several recent retrograde rabies tracing studies targeting different cell classes in the medial prefrontal cortex[33,50], visual cortex[51–53], or somatosensory cortex[19]. Across target areas, both VISp and HVAs receive the most inputs from isocortex, followed by thalamus and HPF (Figure 3a). Strong cortical inputs are often from source areas that receive strong visual area inputs, indicating reciprocal connections between visual cortex and other cortical modules (Figure 4a–b, Extended Data Figure 7d–e). Each target area in visual cortex exhibits unique input patterns, distinguishing dorsal stream HVAs from ventral stream ones, and anterolateral HVAs from anteromedial ones (Figure 3b–e).

Under the overall similar global input patterns, we also observe quantitative differences in inputs to layer- and Cre-defined starter cell classes (Figure 4a,c, Extended Data Figures 6, 7d,f)[47,48,54]. In VISp, compared to excitatory neurons in other layers, L4 excitatory neurons receive the highest inputs from LGd and lowest inputs from higher-order association cortical areas. Similarly, VISl L4 excitatory neurons receive the highest inputs from LP and lowest inputs from association cortical areas. L4 neurons also contribute to the feedforward interareal connections together with L2/3 neurons[55]. For example, SSp-bfd-rll receives inputs preferentially from L4 of VISp and several other HVAs (Extended Data Figure 10)[19].

We find that L6 CT and L6b neurons in VISp, as well as in HVAs, receive significantly higher proportions of contralateral cortical inputs than any other layers do (Figure 4a,c,l, Extended Data Figures 6d, 8a–c). VISp L6 excitatory neurons also receive high proportions of inputs from ipsilateral HVAs and RSP (Figure 4c,l), as shown previously[45,46,54]. Previous studies revealed two major subclasses of excitatory neurons in L6 with distinct output projection patterns, the corticocortical projecting intratelencephalic (IT) subclass and the corticothalamic projecting (CT) subclass[31,45]. Diversity in input connectivity was also shown between these two L6 subclasses in VISp, with L6 IT receiving predominantly local inputs and L6 CT receiving higher proportions of inputs from HVAs and RSP[45,46]. Our results confirmed the strong inputs from HVAs and RSP to L6 CT neurons, but we have not investigated the inputs to L6 IT neurons. Interestingly, the contralateral presynaptic input neurons to L6 neurons in VISp and HVAs were mainly located in deep layers (L5 and L6) (Extended Data Figure 8d), indicating that interhemispheric connectivity is mainly mediated by the callosal projecting L5 IT neurons[20,56] and L6 IT neurons[31,52]. Together, these findings suggest that L6 excitatory cell classes in visual cortex have unique connectivity patterns and are main players in bridging connectivity between two hemispheres as well as linking interhemispheric inputs with the feedback inputs from higher cortical areas.

Among the inhibitory interneurons, we also find that inputs to interneurons are mainly determined by target area and layer distribution of starter cells (Figure 5). Our observation is in line with a recent rabies tracing study which found strong similarity in local and long-range inputs to L2/3 excitatory and inhibitory neuron types[54]. Consistent with the L6 excitatory neurons, interneurons in deep layers also receive higher proportions of contralateral inputs than interneurons in superficial layers. Overall, the comprehensive retrograde connectomes presented in this study provide a foundational resource for more refined investigation of the circuit functions of different neuronal classes in visual cortex.

Hierarchical organization and subnetworks of the visual cortex

In this study we explored the possibility of predicting the hierarchical positions of mouse visual cortical areas by the laminar distribution patterns of presynaptic neurons, an alternative approach from prediction based on laminar termination patterns of axon projections[20]. The feedforward and feedback connections in the mouse visual areas are gauged by the ratio of L2/3/4 inputs to L2/3/4/5 inputs. Using this quantitative parameter, we obtain a hierarchy of the visual areas, which places VISp at the bottom, and VISa and VISpor at the top of the hierarchy in the dorsal stream and the ventral stream, respectively (Figure 7). This hierarchy is largely consistent with those derived from axon termination patterns[20,57], and the anatomical hierarchy revealed by both output and input connectivity patterns mirrors the functional hierarchical organization of mouse visual cortical areas[58].

Our retrograde tracing shows VISa at the top of dorsal stream hierarchy, which is different from anterograde tracing showing VISam at the top. It's worth noting that VISa in mouse dorsal stream has larger receptive field than VISam[24], and VISa doesn't have a complete visual field, whereas VISam does[25,26]. Our current study also identifies two subnetworks in the dorsal stream; the dorsolateral subnetwork consists of anterolateral areas of VISal, VISrl, SSp-bfd-rll and VISa and receives major inputs from cortical and thalamic areas in the somatomotor module, whereas the dorsomedial subnetwork consists of medial areas of VISam and VISpm and receives major inputs from cortical and thalamic areas in the medial association module (Figure 3b–e). There is a gradual transition between the two subnetworks with VISa being the transitional area between them. These unique features of VISa support our current finding that VISa is higher in hierarchical level than VISam.

Our retrograde connectomes also reveal other transitional areas (Figure 3b–e). SSp-bfd-rll is physically located in somatosensory cortex, barrel field, and receives abundant thalamic inputs from VPM. SSp-bfd-rll also has strong reciprocal connections with VISp and other dorsolateral HVAs[59], making it a transitional area between visual and somatosensory systems. VISal has reciprocal connections with both dorsolateral and ventral HVAs, and receives inputs from both somatomotor and lateral cortical modules, making it a transitional area between dorsolateral and ventral networks. Similarly, VISpm is strongly interconnected with VISam, VISp and VISl, and to a lesser extent with other ventral HVAs, and receives inputs from medial module strongly but also from lateral module. Thus, VISpm is a transitional area between dorsomedial and ventral networks[60].

VISpor sits at the top of the ventral stream hierarchy within the cortical network. It also receives strong inputs from LP and possibly direct inputs from SCs (Figure 3h–i), supporting its involvement in the colliculo-cortical pathway that is independent of the geniculo-cortical pathway[39]. VISpor also receives substantial inputs from its neighboring HPF region (Figure 3a).

Overall, our comprehensive retrograde connectomes have enabled a systematic investigation of the network structure of the mouse visual cortical system, revealing specific pathways and areas at the intersections of different pathways. These results suggest that the mouse visual cortex is more complex than a simple two-stream system. There are several topographically organized and continuously varying subnetworks mediated by the HVAs surrounding VISp.

These subnetworks likely play key roles in integrating visual function with a variety of other cortical and subcortical systems.

METHODS

All experimental procedures related to the use of mice were approved by the Institutional Animal Care and Use Committee of the Allen Institute for Brain Science, in accordance with NIH guidelines.

Outline of the data generation and processing pipeline

The AAV helper virus and the monosynaptic rabies tracer were sequentially injected to the same target site with a three-week interval, followed by imaging of the whole brain one week after rabies infection. As this study focused on the visual cortex, our target site identification was mostly guided by intrinsic signal imaging (ISI) of the visual areas. To repeat injections that failed repeatedly under the guidance of ISI as well as to add replicates to expand our data set, additional experiments were conducted using stereotaxic injection coordinates specific for each target site. Rabies-labeled brains were imaged using serial 2-photon tomography (STPT) at every 100 μm, with a total of 140 images for each brain. Injection site polygons were manually drawn based on the expression of dTomato from the AAV helper virus, and the centroids of injection site polygons were later used to verify and assign the injection target areas. Image series were processed in the informatics pipeline for automatic segmentation of signal and registration to the Allen Mouse Brain Common Coordinate Framework version 3 (CCFv3)[22] for subsequent data analyses. Brain sections were collected after STPT and those around the injection sites were further immunostained to enhance the dTomato signal. Starter cells were quantified after confocal imaging of the stained sections. Rigorous manual quality control steps were conducted to exclude experiments with noticeable tissue damage, injection failure, imaging failure or segmentation errors.

Animals

To identify presynaptic inputs to different neuronal populations in the visual cortex, we used 18 Cre-transgenic mouse lines (in congenic C57BL/6J background, aged 2-6 months, either gender depending on availability), Emx1-IRES-Cre (JAX 005628, Kevin Jones)[61], Sepw1-Cre_NP39 (MMRRC 036190, Nathaniel Heintz and Charles Gerfen)[62], Cux2-IRES-Cre (MMRRC 031778, Ulrich Mueller)[62], Nr5a1-Cre (JAX 006364, Brad Lowell)[63], Tlx3-Cre_PL56 (MMRRC 036547, Nathaniel Heintz and Charles Gerfen)[64], A93-Tg1-Cre (JAX 017346, Allen Institute for Brain Science)[65], Rbp4-Cre_KL100 (MMRRC 031125, Nathaniel Heintz and Charles Gerfen)[64], Ntsr1-Cre_GN220 (MMRRC 030648, Nathaniel Heintz and Charles Gerfen)[64], Syt6-Cre_KI148 (MMRRC 032012, Nathaniel Heintz and Charles Gerfen)[64], Ctgf-2A-dgCre (JAX 028535, Allen Institute for Brain Science)[65], Gad2-IRES-Cre (JAX 010802, Z. Josh Huang)[66], Ndnf-IRES2-dgCre (JAX 028536, Allen Institute for Brain Science)[65], Pvalb-IRES-Cre (JAX 008069, Silvia Arber)[67], Sst-IRES-Cre (JAX 013044, Z. Josh Huang)[66], Vip-IRES-Cre (JAX 010908, Z. Josh Huang)[66], Chat-IRES-Cre (JAX 006410, Brad Lowell)[68], Htr3a-Cre_NO152 (MMRRC 036680, Nathaniel Heintz and Charles Gerfen)[64], and Calb1-IRES2-Cre (JAX 028532, Allen Institute for Brain Science)[65].

These Cre lines had been previously utilized together with anterograde AAV viral tracers for the construction of the Allen Mouse Brain Connectivity Atlas. The expression patterns of these lines can be found in the Allen Institute Transgenic Characterization data portal (http://connectivity.brain-map.org/transgenic). To quantify the spurious rabies virus labeling, wild-type C57BL/6J mice were used. To compare different recombinant rabies and AAV helper viruses, Cre transgenic mice labeling neurons and non-neuronal cells were used. We used three non-neuronal Cre lines to validate the monosynaptic retrograde tracing system, Olig2-Cre (JAX stock number 025567, William Richardson)[69], Tek-Cre (JAX 004128, Richard Flavell)[70], and Aldh1l1-CreERT2 (JAX 023748, Nathaniel Heintz)[71], which express Cre in oligodendrocytes, vascular endothelium, and astrocytes, respectively. Male and female adult mice aged 78-155 days old (median of 90 days old) were used for experiments. The specific genotypes, genders and ages of mice used for each experiment are listed in Supplementary Tables 1 and 2. Mice were housed under 14h:10h light-dark cycle with ad libitum access to food and water.

Virus design, preparation and titer information

The cell line used for AAV production was HEK293T cells (ATCC, CRL-11268). The cell lines used for rabies virus production and titration were HEK293t-TVA800 cells, B7GG cells, and BHK-EnvA cells (Callaway lab, The Salk Institute for Biological Studies), and N2A-N2c(G) and N2A-EnvA_cytG cells (Jessell lab, Columbia University).

AAV viruses and rabies viruses used in the mesoscale retrograde connectome pipeline were generated at the Allen Institute for Brain Science. The AAV helper viruses utilize the Cre-dependent FLEX strategy and contain the tricistronic cassettes of Syn-DIO-TVA-dTomato-RV G, followed by a short bovine growth hormone polyadenylation sequence. The Kozak sequence and the start codon of TVA are located 5’ to the FLEX switch, while the TVA (lacking a start codon)-P2A-dTom-P2A-RV G cassette is within the FLEX cassette and inverted respective to the promoter. The AAV helper virus selected for the mesoscale retrograde connectome pipeline utilizes a mutant TVA, TVA^{66T}, and the RV G from the CVS N2c strain.

The AAV1 serotype of the helper virus was produced using a helper-free HEK293 cell system followed by iodixanol gradient purification. Multiple batches of AAV1-Syn-DIO-TVA^{66T}-dTom-CVS N2c G virus were used in the course of the mesoscale connectivity project, and the titers of the virus preps were in the range of 2×10^{12} to 1×10^{13} GC/ml.

The CVS N2c$^{\Delta G}$-H2B-EGFP rabies virus was generated by replacing GFP in the rabies genomic plasmid RabV CVS-N2c(deltaG)-EGFP (Addgene, Plasmid #73461) with H2B-EGFP flanked by 5’ XmaI and 3’ NheI-KasI sites. EnvA CVS N2c$^{\Delta G}$-H2B-EGFP rabies virus was generated from the genomic plasmid as described previously[16]. The titers of EnvA CVS N2c$^{\Delta G}$-H2B-EGFP rabies virus preps used in the study were adjusted to be around 5×10^9 GC/ml.

The SAD B19$^{\Delta G}$-H2B-EGFP virus was generated by inserting the H2B-EGFP sequence into the gG locus of the pSADdeltaG-F3 plasmid (Addgene, Plasmid #32634). The EnvA SAD B19$^{\Delta G}$-H2B-EGFP rabies virus was generated from the genomic plasmid as described previously[72]. The EnvA SAD B19$^{\Delta G}$-GFP virus was obtained from the Salk Institute. Both EnvA SAD B19$^{\Delta G}$-H2B-EGFP and EnvA SAD B19$^{\Delta G}$-GFP viruses were diluted to 5 x 10^9 GC/ml to match that of the EnvA CVS N2c$^{\Delta G}$-H2B-EGFP virus.

Surgery

All mice received unilateral injections into a single target region in the left hemisphere (except that twelve mice received injections in the right hemisphere). For monosynaptic retrograde tracing of whole brain inputs to Cre-defined cell populations, the AAV helper virus was injected first into the target site, followed 3 weeks later by another injection in the same location with the EnvA CVS N2c$^{\Delta G}$-H2B-EGFP rabies virus. After one week survival, animals were sacrificed, and perfused with 4% paraformaldehyde (PFA). Brains were dissected and post-fixed in 4% PFA at room temperature for 3–6 h and then overnight at 4°C.

To precisely target each visual area, functional mapping of visual field space by intrinsic signal imaging (ISI) was used to guide injection placement[20]. An image of the surface vasculature was acquired to provide fiduciary marker references on the surface of the brain. An overlay of the visual field map over the vasculature fiducials was used to identify the target injection site. For injections that failed repeatedly under the guidance of ISI, transcranial injections were conducted using stereotaxic injection coordinates specific for each target site. The anterior/posterior (AP) coordinates are referenced from the transverse sinus (TS), the medial/lateral (ML) coordinates are distance from midline at Bregma, and the dorsal/ventral (DV) coordinates are measured from the pial surface of the brain. Stereotaxic coordinates for each area are as follows: VISp (6 subareas) (VISp-1: AP:1.50(TS), ML: −2.55, and DV:0.3, 0.6; VISp-2: AP:2.59(TS), ML:−2.55, and DV:0.3, 0.6; VISp-3: AP:1.90(TS), ML:−3.10, and DV:0.3, 0.6; VISp-4: AP:1.05(TS), ML:−3.50, and DV:0.3, 0.6; VISp-5: AP:0.75(TS), ML:−3.00, and DV:0.3, 0.6; VISp-6: AP:0.61(TS), ML:−2.10, and DV:0.3, 0.6), VISl (AP:1.4(TS), ML: −4.10, DV:0.3, 0.6); VISpm (AP:1.9(TS), ML: −1.60; DV:0.3, 0.6), VISam (AP: 3.0(TS), ML: −1.70, DV:0.3, 0.6), VISal (AP: 2.4(TS), ML: −3.70, DV:0.3, 0.6, Angle:15°), and VISrl (AP: 2.8(TS), ML:−3.30, DV: 0.3, 0.6). For some target areas, injections were made at two depths to label neurons throughout all six cortical layers. The AAV1 helper virus was injected using the iontophoresis method, with current settings of 3 μA, 7 sec on/off cycles and 5 min total. The EnvA rabies virus was injected using a nanoinjector, and a total of 500 nl was delivered in 23 nl increments over a 3 min and 10 sec interval.

Tamoxifen-inducible Cre line (CreER) mice were treated with 0.2 mg/g body weight of tamoxifen solution in corn oil via oral gavage once per day for 5 consecutive days starting the week following AAV helper virus injection. Trimethoprim-inducible Cre line mice were treated with 0.3 mg/g body weight of trimethoprim solution in 10% DMSO via oral gavage once per day for 3 consecutive days starting the week following AAV helper virus injection. Rabies virus was injected 3 weeks post induction. All mice were deeply anesthetized before intracardial perfusion, brain dissection, and tissue preparation for serial imaging.

Serial two photon tomography

The injected brains were imaged by STPT (TissueCyte 1000, TissueVision Inc. Somerville, MA) as described previously with a few modifications[20,21]. In brief, brains were embedded in agarose block followed by co-embedding with polyacrylamide. Imaging proceeded along the rostral-caudal axis beginning from the caudal end of the brain. The specimen was illuminated with 925 nm wavelength light. Two-photon image tiles for red and green channels with a nominal resolution of 0.875 µm x 0.875 µm x 2 µm x-y-z were taken at 40 µm below the cutting surface. The laser power and photo-multiplier tube (PMT) voltage were set at 190 mW (measured at the objective) and ~600 V (equal on all channels). In order to compensate for variation between imaging systems and specimens, these parameters are adjusted on each imaging run using an observed level of autofluorescence in the red channel. The following procedures were conducted: locate the central canal of the brain stem; locate the surface of the tissue; adjust the objective piezo stage such that the image plane is 40 µm deep in the specimen; move 700 µm laterally, exposing an area of uniform tissue structure; adjust the PMT voltage such that the mean intensity of this area falls within the range of 600-650; from the central canal, the specimen is then centered laterally within the imaging area and the acquisition is commenced. After an entire brain section was imaged, a 100-µm section was removed from the specimen by the vibratome, followed by imaging of the next plane. Scanned image tiles were stitched to form a single high-resolution image. Images from 140 sections were collected to cover the full range of mouse brain. Upon completion of imaging, sections were retrieved and stored in PBS with 0.1% sodium azide at 4°C.

Starter cell identification and quantification

The starter cells are those with both AAV helper virus and EnvA RV-H2B-EGFP infection, and thus have red fluorescence in the soma and green fluorescence in the nuclei. For starter cell quantification, TissueCyte brain sections were sorted according to the rostrocaudal axis. Around 20 100-µm sections flanking the virus injection sites were identified, mounted on gelatin coated glass slides, and immunostained to enhance dTomato red fluorescence signal. The immunofluorescence staining was conducted using an automated slide stainer (Biocare, IntelliPATH FLX). Slides were blocked in Image iT FX Signal Enhancer (Thermo Fisher Scientific Cat# I3693) for 45 minutes, followed by 1-hour incubation in a blocking solution containing 1% normal goat serum (Vector Laboratories Cat#S1000) and 1% Triton X (VWR). Sections were then incubated in the anti-RFP primary antibody solution (1% goat serum, 1% Triton X, Rockland Cat# 600-401-379, RRID:AB_2209751, 1:2000) for 1.5 hours, and then in the secondary antibody solution (1% goat serum, 1% Triton X, and 1:500 goat anti-rabbit conjugated with Alexa Fluor 594, Thermo Fisher Scientific Cat# A-11012, RRID:AB_2534079) for 2 hours at room temperature after rinsing with 0.1% Triton X wash solution. All sections were stained with 5 µM DAPI (Thermo Fisher Scientific D1306) and coverslipped using Fluoromount G (Southern Biotech Cat# 0100-01B). Stained sections were imaged using a Leica SP8 TCS confocal microscope under a 10x objective. Starter cells were counted in ImageJ using the Cell Counter plugin. We manually delineated layers 1 to 6, using the DAPI staining fluorescence and background fluorescence in each image, and assigned starter cells to layers 1, 2/3, 4, 5, and 6.

Image data QC and annotation

The acquired TissueCyte STPT images and the confocal images went through several steps of quality control processes: annotation QC, staining QC, starter cell QC, and segmentation QC. Specimens that did not pass any one of the QC steps were considered fails and removed from the pipeline. After TissueCyte imaging, specimens were assessed for surgical and imaging quality through Annotation QC. Failures at this step included no green signal, TissueCyte imaging error, tissue damages, and poor surgical targeting. Tissue damages at the injection sites were classified into 5 levels, None (no damage detected), Very minor (1 section with detectable damage usually at brain surface), Minor (1-3 sections with detectable damage usually at brain surface), Moderate (3-6 sections with damage effecting cortical layers or signal with damage possibly effecting starter cells), and Severe (significant damage to tissue and signal in multiple sections). Specimens with moderate damage were followed up by inspecting slides/confocal images, and those with damages affecting starter cells were failed. Specimens with severe damages were failed. Polygons were drawn around the injection site to link the injection site to the Allen Mouse Brain Common Coordinate Framework, version 3 (CCFv3). Specimens having passed Annotation QC were sent for the next step of mounting, and immunostaining for starter cell identification. Staining QC identified and removed specimens in which no red-fluorescent cells were found after immunostaining-mediated enhancement of red fluorescence signal from the AAV helper virus. Starter cell QC further removed specimens in which no starter cells were identified after confocal imaging. Finally, specimens with errors in the subsequent informatics data pipeline steps were identified in the Segmentation QC step.

Image data processing

STPT images were processed and registered to the CCFv3 through our informatics data pipeline (IDP)[22,23]. The signal detection algorithm was modified to detect nuclear objects with high sensitivity, which accepts out-of-focus nuclei and has lower contrast requirements. In addition, high intensity pixels near the detected objects were included into the signal pixel set. Detected objects near hyper-intense artifacts occurring in multiple channels were removed. The output was a full resolution mask that classified each pixel as either signal or background. An isotropic 3D summary of each brain was constructed by dividing each image series into 10 μm × 10 μm × 10 μm grid voxels. Total signal was computed for each voxel by summing the number of signal-positive pixels in that voxel. Each image stack was registered in a multi-step process using both global affine and local deformable registration to the 3D CCFv3 as previously described[22,23].

Analysis of whole brain presynaptic inputs to the visual areas

The accuracy of targeting was verified by overlaying the injection site polygon of each experiment to the ISI image or by identifying the anatomical structure where the injection centroid was located in the CCFv3. Since the signal detection algorithm was optimized to detect sparse presynaptic labeling with high sensitivity, the automatically detected volume of input signal can have false positives where high background signal is falsely identified as input signal. False positives tend to occur more frequently in brain structures with low input signal and high background fluorescence such as the cerebellum and are rarely found in areas with strong input signals such as the isocortex. In order to remove this type of artifacts, we identified a set of 92 negative brains that were processed through the pipeline, but showed no rabies-mediated GFP expression, and used this negative dataset to calculate the threshold of false positive signal, i.e., the value of mean input signal volume plus 6 standard deviations for each of the 314 ipsilateral and 314 contralateral major structures of the brain. Any structure not passing this threshold was set to “0”. A manually validated binary mask was then applied to further remove artifacts in informatically-derived measures. Following these two steps, input signal volume in a given structure was normalized to the total inputs of the brain. The post-threshold, masked, normalized input signal volumes were used to build the weighted connectivity matrix.

Using automated image registration to CCFv3, we quantified input signal by layer within each cortical target. This automatic quantification process assigned input signal volume to layers 1, 2/3, 4, 5, 6a and 6b. Input signals in layers 6a and 6b were combined to represent input signals in layer 6. When analyzing the fraction of inputs in a given cortical area across layers, the threshold for per structure input signal volume was set at 0.0004. Any structure below this threshold was set as “0”, and no fraction of layer inputs was calculated. This threshold value is higher than 99% of input signal volumes measured for structures in the negative dataset and is equivalent to ~10 labeled cells based on our comparison of input signal volume and manual counting. We reasoned that cortical areas below this threshold had very sparse RV-labeled neurons, which could lead to extreme values when calculating the layer-specific contribution of inputs.

Hierarchical clustering in Figure 2 was conducted using the pvclust package (pvclust_2.2-0) in R (R version 3.6.0). The agglomerative method used in hierarchical clustering was “ward.D”, and the distance measure used was correlation. The R software was used for statistical tests and generation of graphs.

Estimation of hierarchical levels

We first identified a quantitative hierarchical parameter h based on the anatomical features of feedback and feedforward connections, with h calculated as the ratio of layers 2/3/4 inputs to layers 2/3/4/5 inputs. We used the linear regression analysis to estimate a set of hierarchical levels that best predict the measured h values. A model can be specified as $Y = X\beta$, wherein Y is a vector containing the h values of all source areas to each target, β contains the estimated hierarchical levels assigned to each area, and X is the incidence matrix. X is constructed so that each column corresponds to one of the 43 cortical areas and each row corresponds to a connection between two areas. All of the elements of a row are zero except in the two columns corresponding to the areas participating in the connection, with the source area taking the value of −1 and the target area taking the value of 1. The hierarchical level of the primary visual area was set at zero.

Limitations of rabies virus tracing and data analysis methods

The monosynaptic rabies virus tracing system is a powerful tool in its ability to selectively infect starter cells and label only the first-order presynaptic neurons. However, although we have improved our virus tools to further enhance specificity and efficiency, there are still limitations of this strategy, which should be taken into consideration when interpreting the results.

Due to the high affinity between TVA and EnvA, low-level leaky expression of TVA in the absence of Cre is sufficient for rabies infection[8,11,13,73]. Although the leaky expression of RG is often too low to allow trans-synaptic transportation of rabies virus, these cells can be mistakenly counted as local trans-synaptically labeled cells. Our AAV helper virus is specifically designed to reduce spurious expression in the absence of Cre by utilizing $\text{TVA}^{66\text{T}}$, and rare labeling in wild type animals are restricted to the injection site. However, AAV1 serotype can transport retrogradely along the axon at a low frequency. It is possible that the AAV helper virus can infect neurons in a brain area with direct input to the visual area, in effect creating new starter cells if the Cre-driver line in use also has expression there, leading to the labeling of neurons in upstream areas without direct connection with the visual area. Therefore, independent connection mapping strategies are required to verify novel connections revealed by rabies tracing.

The mechanisms by which rabies viruses are transported across synapses, as well as the tropism of cell types and synapse types, are not fully understood. It is possible that the rabies virus tracing system does not reveal all presynaptic neurons, even though we used the CVS N2c strain which has higher trans-synaptic efficiency. Rabies virus may not cross all synapses with equal efficiency, leading to preferential representation of certain cell types within the presynaptic connectome. The efficiency of trans-synaptic spread of rabies virus is also affected by the expression level of RG in the starter neurons, which is in turn limited by the expression of Cre from the driver lines, the titers of the AAV helper virus and rabies virus tracer, as well as the number of viral particles successfully delivered to the target sites.

We applied our informatics pipeline to automatically register image series to the CCFv3 and quantify whole-brain input signals. Our method allows us to compare input patterns across different experiments, but it falls short of direct counts of presynaptic cells per brain structure. The automatic signal detection process can generate false positive signals which are background signals picked up as input signals. We subtracted a standard threshold from all experiments in an attempt to remove false positive signals, which do not take into consideration background variations among different experiments.

We conducted comparisons across experiments using fractions of the whole-brain total inputs, which reduce variability between experiments. This normalization method is the more appropriate approach than normalizing by the number of starter cells, because of the non-linear relationship between the numbers of starter cells and input cells due to the existence of convergent and divergent connections (that can also be variable between cell types). However, normalization using fractions of total inputs could lead to overestimated fractions of inputs from major source areas in experiments with small numbers of starter cells, as well as underestimating the fraction of inputs per brain structure for cell types receiving broader inputs across the brain.

Statistics & Reproducibility

No statistical method was used to predetermine sample size. However, our previous studies demonstrated that n=1 experiment per source area and Cre line is sufficient to reveal the anterograde projectome[20,21]. We therefore included in our retrograde connectome experiments with n>=1 per target and Cre lines. Specimens that did not pass the quality control processes of our pipeline were excluded. The experiments were not randomized. The Investigators were not blinded to allocation during experiments and outcome assessment, because imaging and informatic processing were automatically processed and quantified, and the results were quantitative and did not require subjective judgment. Data distribution was assumed to be normal, but this was not formally tested.

Extended Data

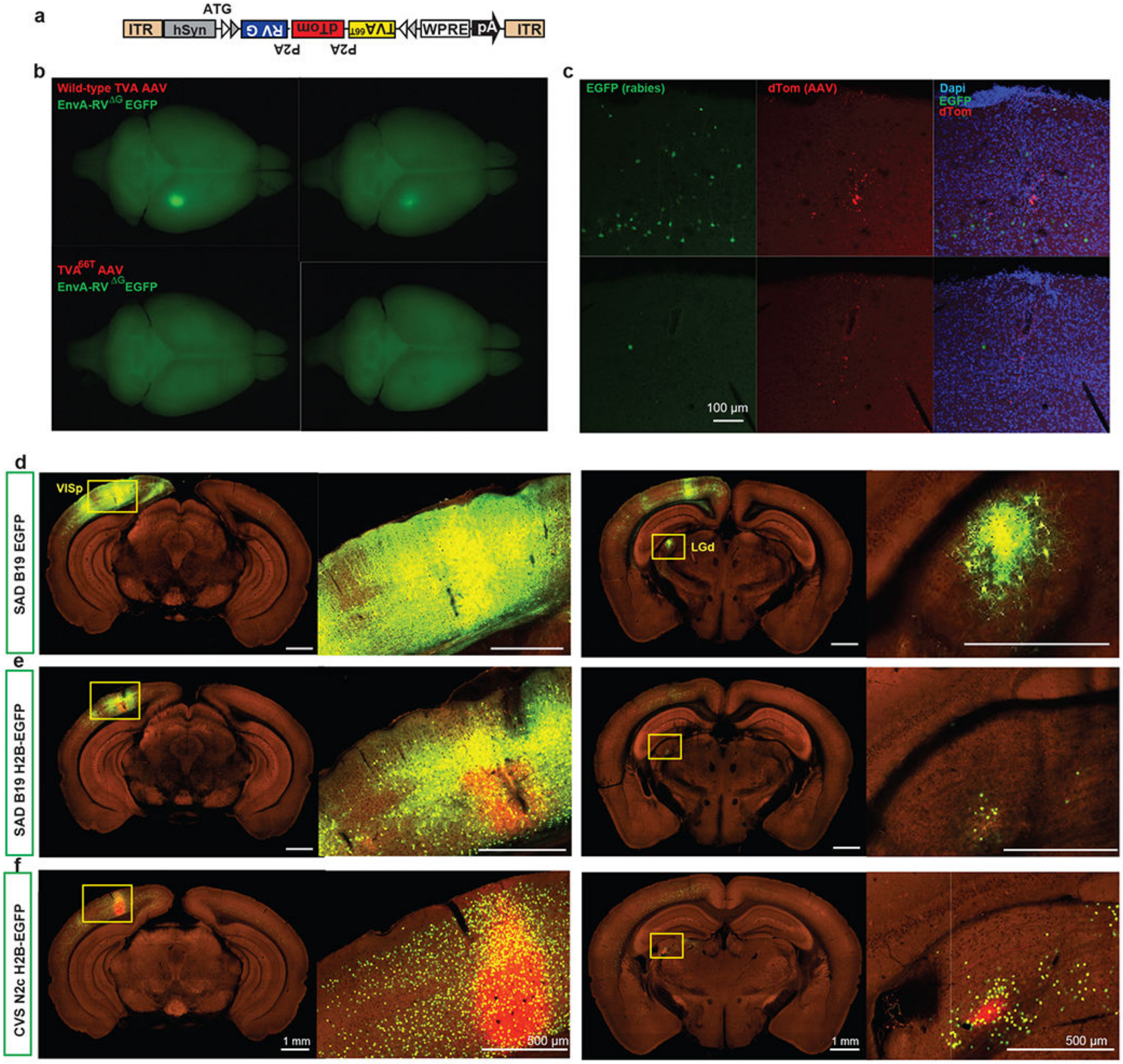

Extended Data Figure 1. Comparison of different AAV helper viruses and rabies viruses for monosynaptic retrograde tracing.

(a-c) Comparison of spurious rabies infection from AAV helper viruses expressing wild-type TVA and mutant TVA^{66T}. Tricistronic AAV helper viruses were constructed to conditionally express either the wild-type TVA or TVA^{66T}, together with dTomato and RG (a). Cre-negative wild-type mice were sequentially injected with AAV helper viruses and EnvA-pseudotyped recombinant rabies viruses expressing EGFP. Each AAV helper virus/rabies virus pair was tested in two wild-type mice. Top-down view of whole brains (b) and observation of the injection sites under the confocal microscope (c) revealed fewer spurious rabies infection from AAV helper virus expressing TVA^{66T}. **(d-f)** Comparison of monosynaptic retrograde tracing in VISp using SAD B19 strain of recombinant RV expressing EGFP (d, similar results observed in 6 independent experiments) or H2B-EGFP (e, similar results observed in 7 independent experiments) or CVS N2c strain of recombinant RV expressing H2B-EGFP (f, similar results observed in 303 experiments). Note that in H2B-EGFP expressing SAD B19 experiment there is still green fluorescence in the processes of infected and transmitted neurons (e), due to the very high-level transgene expression in this rabies strain, whereas in CVS N2c experiment H2B-EGFP is strictly contained within nuclei of infected and transmitted neurons (f). Scale bars, 100 μm in b, 1 mm in panels showing full brain sections in d-f, and 500 μm in panels showing selected brain areas in d-f.

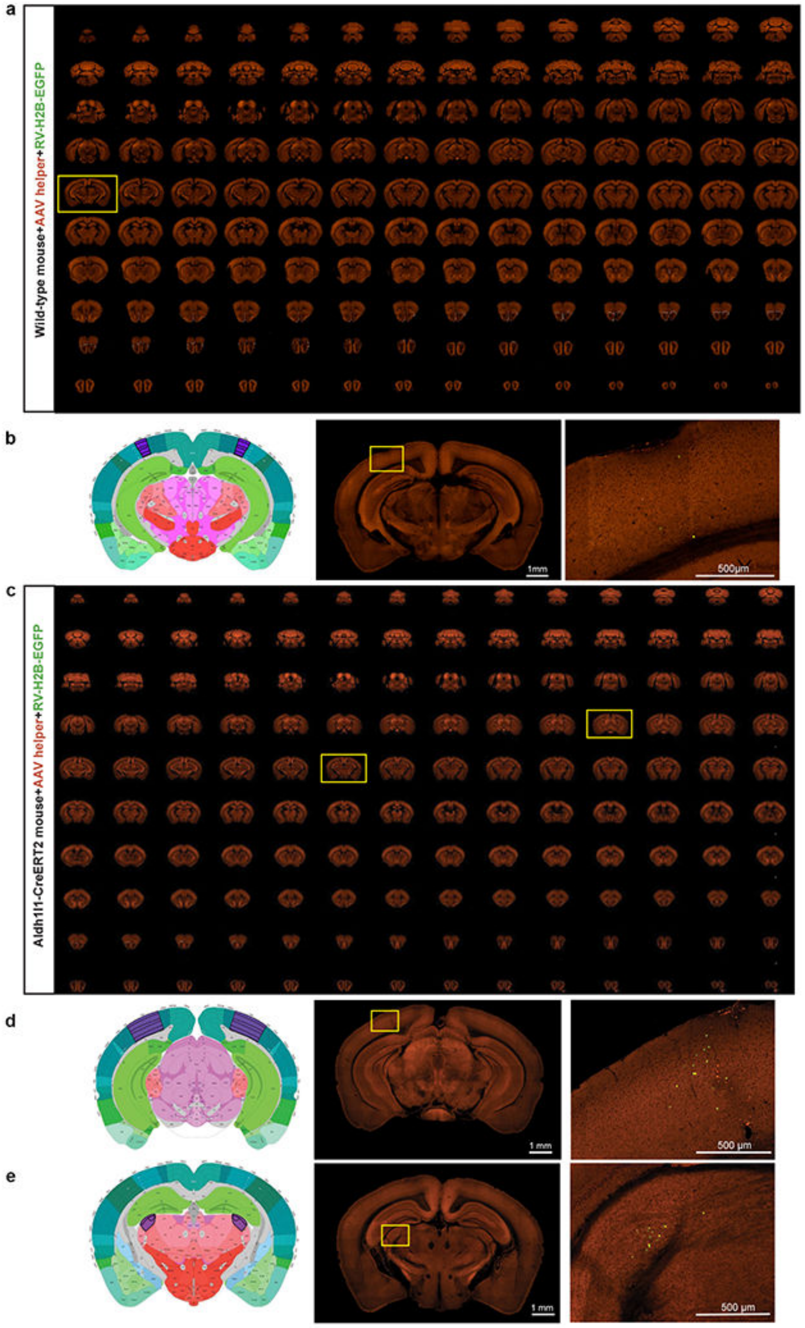

Extended Data Figure 2. Validation of the AAV helper virus and recombinant rabies used in the retrograde connectomic pipeline in wild-type mice and non-neuronal Cre lines.

(a) Sequential two-photon images of a Cre-negative wild-type mouse brain injected with the AAV helper virus and EnvA-pseudotyped CVS N2c$^{\Delta G}$ rabies virus expressing H2B-EGFP. Similar results observed in 3 independent experiments. **(b)** Absence of RV-labeled neurons except a few H2B-EGFP-expressing cells in the injection site. Virus injection was targeted to VISp and validation was conducted in two wild-type mice. Left and middle panels: corresponding 2D atlas plate of Allen CCFv3 and the section image from the outlining box in a showing the injection site. Right panel: Image magnified from the box in the middle panel. Applying the monosynaptic rabies tracing to wild-type mice led to only a few H2B-EGFP-labeled cells in the injection site, but no starter cells in the injection site and no H2B-GFP-labeled cells outside the injection site. This shows that our system does not have the issue of spurious local rabies virus uptake due to low-level expression from the AAV helper in the absence of Cre, or local infection by small quantities of non-pseudotyped, RG-coated RV^{dG} virus particles that may be present in the EnvA-pseudotyped rabies virus preparation. We then confirmed that the trans-synaptic transfer of the recombinant rabies relies on the expression of rabies G from the AAV helper. A G-minus version of the AAV helper virus, which conditionally expresses TVA^{66T} and dTomato after Cre-mediated recombination, was injected into Cre^+ mice, followed by the injection of rabies virus three weeks later. We observed H2B-EGFP-labeled cells only at the injection site and nowhere else in the brain. This finding confirms that the presynaptic labeling is specific for the Cre^+ starter cells expressing the tricistronic cassette and infected with the RV-H2B-GFP rabies virus. **(c)** Sequential two-photon images of rabies labeling in an astrocyte-specific Cre mouse brain injected with hSyn promoter-driven AAV helper virus and recombinant rabies virus into VISp. Similar results observed in 4 independent experiments. **(d-e)** Left and middle two panels: corresponding 2D atlas plates of Allen CCFv3 and the section images from the boxes in c. Right panels: Representative images magnified from the boxes in the middle panels reveal sparse labeling around the injection site (d) and in LGd (e). We tested the monosynaptic rabies tracing system in three non-neuronal Cre lines, Olig2-Cre, Tek-Cre, and Aldh1l1-CreERT2, which express Cre in oligodendrocytes, vascular endothelium, and astrocytes, respectively. Among all experiments using the non-neuronal Cre lines, with either the hSyn-driven AAV helper virus used in the pipeline or a similarly constructed CMV-driven helper virus, sporadic long-distance H2B-EGFP-labeled cells were found only in 50% of the injected Aldh1l1-CreERT2 mice. Our results show that the occasionally infected non-neuronal cells do not support the spread of rabies virus to neurons in local or distant areas.

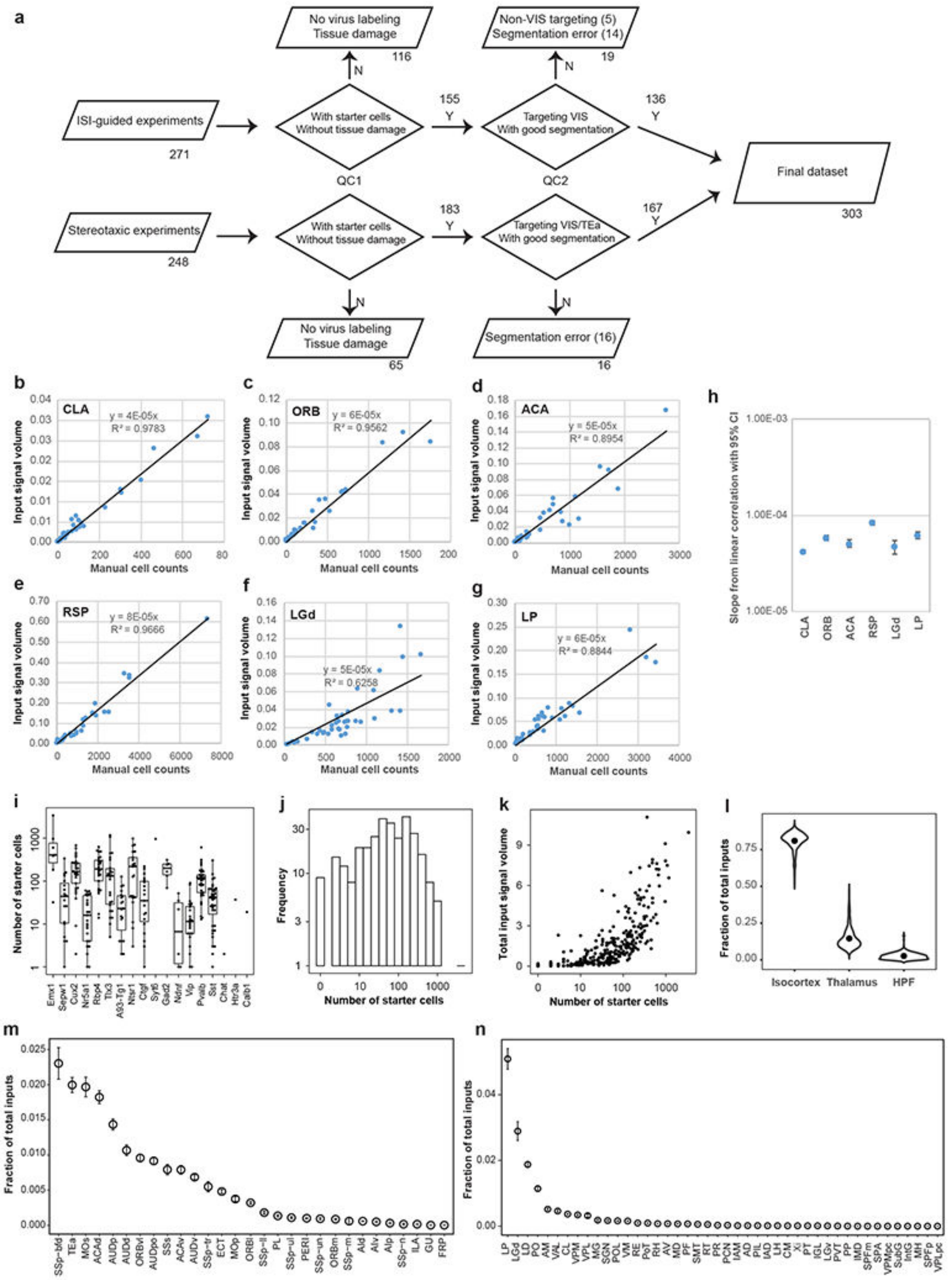

Extended Data Figure 3. Overview of experiments included in the final dataset, automatic input signal detection and characterization of inputs to cell classes defined by Cre lines in the visual cortex.

(a) Flow chart showing the injection methods, and numbers of experiments passing each QC step. QC1 excluded experiments with no rabies virus labeling or with tissue damage. QC2 excluded experiments with segmentation errors that prevent quantitative analysis or with targeting sites falling outside the visual cortex. One experiment targeting TEa was included in the final data set. For experiments guided by ISI, target validation was performed by overlaying injection polygons with sign maps derived from ISI, and overlaying injection centroids in the CCFv3. Inconsistency between ISI-assigned targets and CCFv3-derived targets were observed in 15 out of the total 136 ISI-guided experiments in the final data set. We assigned injection targets based on the overlaying of injection polygons with sign maps. **(b-g)** Relationship between per structure input signal volume measured by the informatics data pipeline and manual cell counts. Linear correlation between input signal volume and manually counted input cells was shown in various brain areas. In the six example structures from cortex, thalamus and cortical subplate, strong positive linear correlations were found between automatic measurement and manual counts (R^2 in the 0.62-0.98 range). **(h)** Slopes from linear correlations between informatically measured input signals and manual cell counts in various brain areas. The numbers of independent experiments are as follows: CLA: n=11; ORB: n=10, ACA: n=11, RSP: n=19; LGd: n=19; LP: n=19. **(i)** Number of starter cells for experiments categorized in Cre lines. Box plots show median and interquartile range (IQR). Whiskers show the largest or smallest value no further than 1.5 × IQR from the hinge. The numbers of independent experiments are as follows: Emx1: n=7, Sepw1: n=19; Cux2: n=29; Nr5a1: n=25; Rbp4: n=25; Tlx3: n=26; A93-Tg1: n=19; Ntsr1: n=21; Ctfg: n=19; Syt6: n=1; Gad2: n=6; Ndnf: n=6; Vip: n=24; Pvalb: n=33; Sst: n=40; Chat: n=1; Htr3a: n=1; Calb1: n=1. **(j)** Distribution of numbers of starter cells across all experiments. **(k)** Relationship between numbers of starter cells and total inputs from the whole brain. **(l)** Fractions of inputs from isocortex, thalamus and HPF to the mouse visual cortex. Dots represent the median values of input signals. **(m-n)** Fractions of total inputs from non-VIS isocortical areas (m) and thalamic areas (n). Brain areas are ordered according to their levels of input signals. Data are shown as mean ± s.e.m. A total of 303 independent experiments were included.

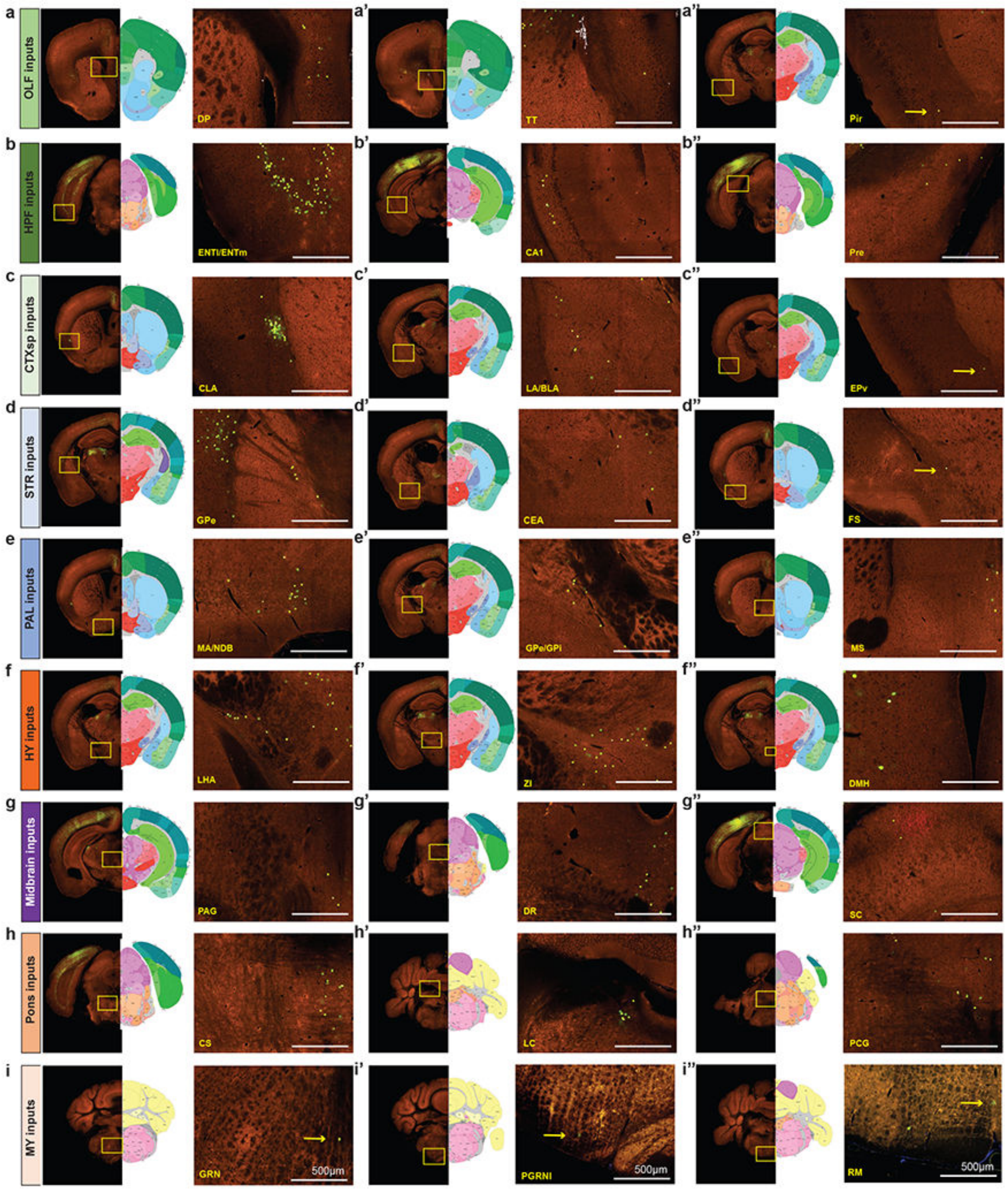

Extended Data Figure 4. Representative images of presynaptic inputs to the visual areas from anatomical structures outside of cortex and thalamus.

Coronal STPT images and their corresponding 2D atlas plates in Allen CCFv3 show labeled presynaptic neurons in OLF (a-a”), HPF (b-b”), CTXsp (c-c”), STR (d-c”), PAL (e-e”), HY (f-f”), MB (g-g”), pons (h-h”), and MY (i-i”). Claustrum (CLA) in CTXsp, diagonal band nucleus (NDB) in PAL, and lateral hypothalamic area (LHA) in HY each represent ~0.1% of whole brain inputs; globus pallidus, external segment (GPe) in PAL, basolateral amygdalar nucleus (BLA) in CTXsp, and zona incerta (ZI) in HY each account for ~0.01% of whole brain inputs; dorsal peduncular area (DP) in OLF, locus ceruleus (LC) in pons, and superior colliculus (SC) in MB each account for ~0.001% of whole brain inputs; areas in MY each account for ~0.0001% of whole brain inputs. Rare inputs in several structures of MY are also found in less than 10% of all experiments (Supplementary Table 3), which could be missed using other connectivity mapping techniques. Clustered inputs are found in NDB (fraction of whole brain inputs in NDB > 0 in 93% of all experiments), substantia innominata (SI) (fraction of whole brain inputs in SI > 0 in 75% of all experiments), LC (fraction of whole brain inputs in LC > 0 in 66% of all experiments), and DR (~0.01% of whole brain inputs, found in 63% of all experiments). The numbers of independent experiments with similar results are 121 in a, 61 in a’, 52 in a”, 254 in b, 165 in b’, 137 in b”, 278 in c, 187 in c’, 149 in c”, 236 in d, 187 in d’, 68 in d”, 226 in e, 110 in e’, 152 in e”, 275 in f, 224 in f’, 198 in f”, 214 in g, 187 in g’, 33 in g”, 231 in h, 193 in h’, 193 in h”, 53 in i, 52 in i’, and 30 in i”. Enlarged views of boxed areas are shown in the right-hand panels for each major brain structure. Arrows highlight the location of single labeled cells.

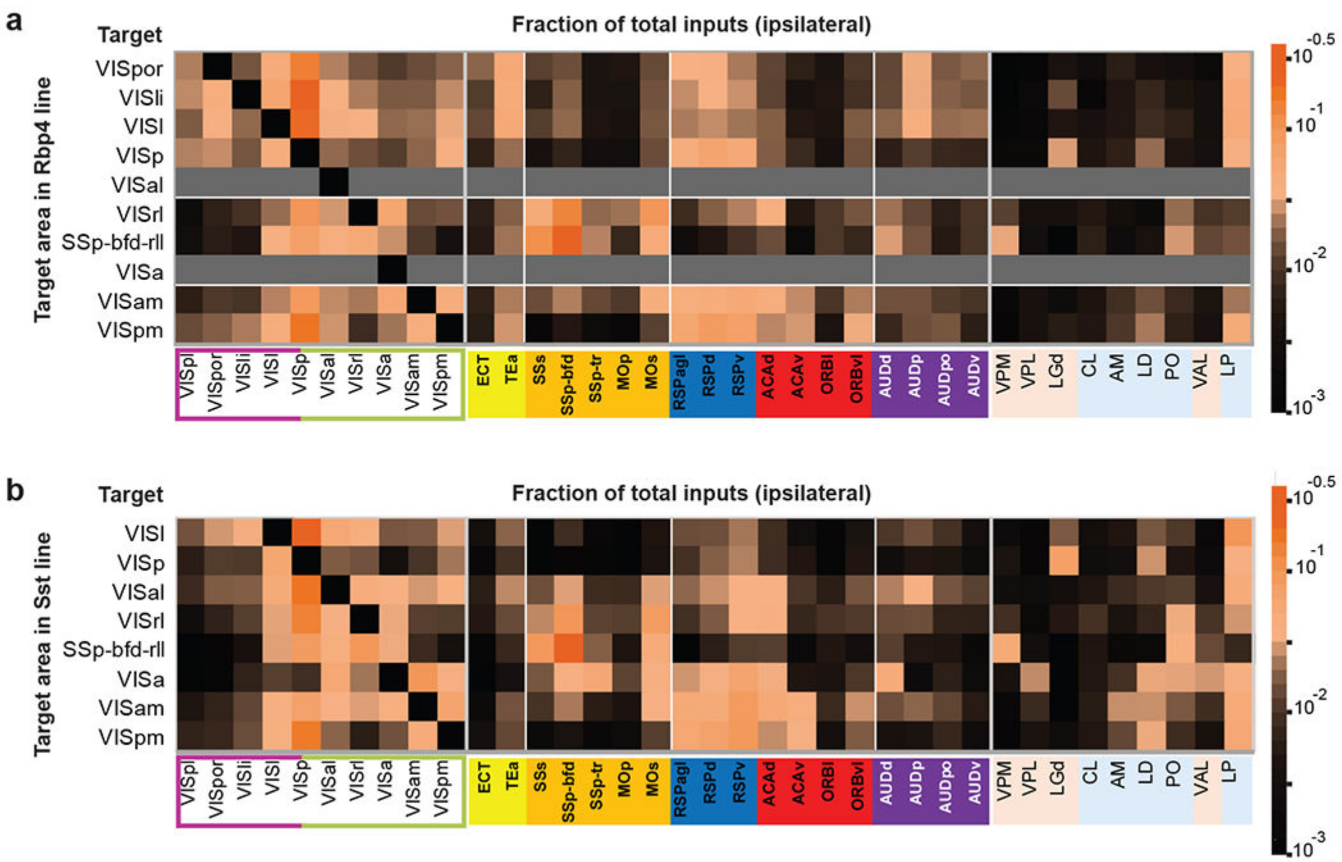

Extended Data Figure 5. Connectivity matrices comparing the inputs to Rbp4 (a) and Sst (b) neurons in the visual areas from within the visual cortex, non-visual isocortical modules, and thalamus.

Gray indicates experiments not available. In the matrix, each row represents experiments with the same target area, and each cell shows the fraction of the total inputs in a given input structure measured from a single experiment or the average when n > 1.

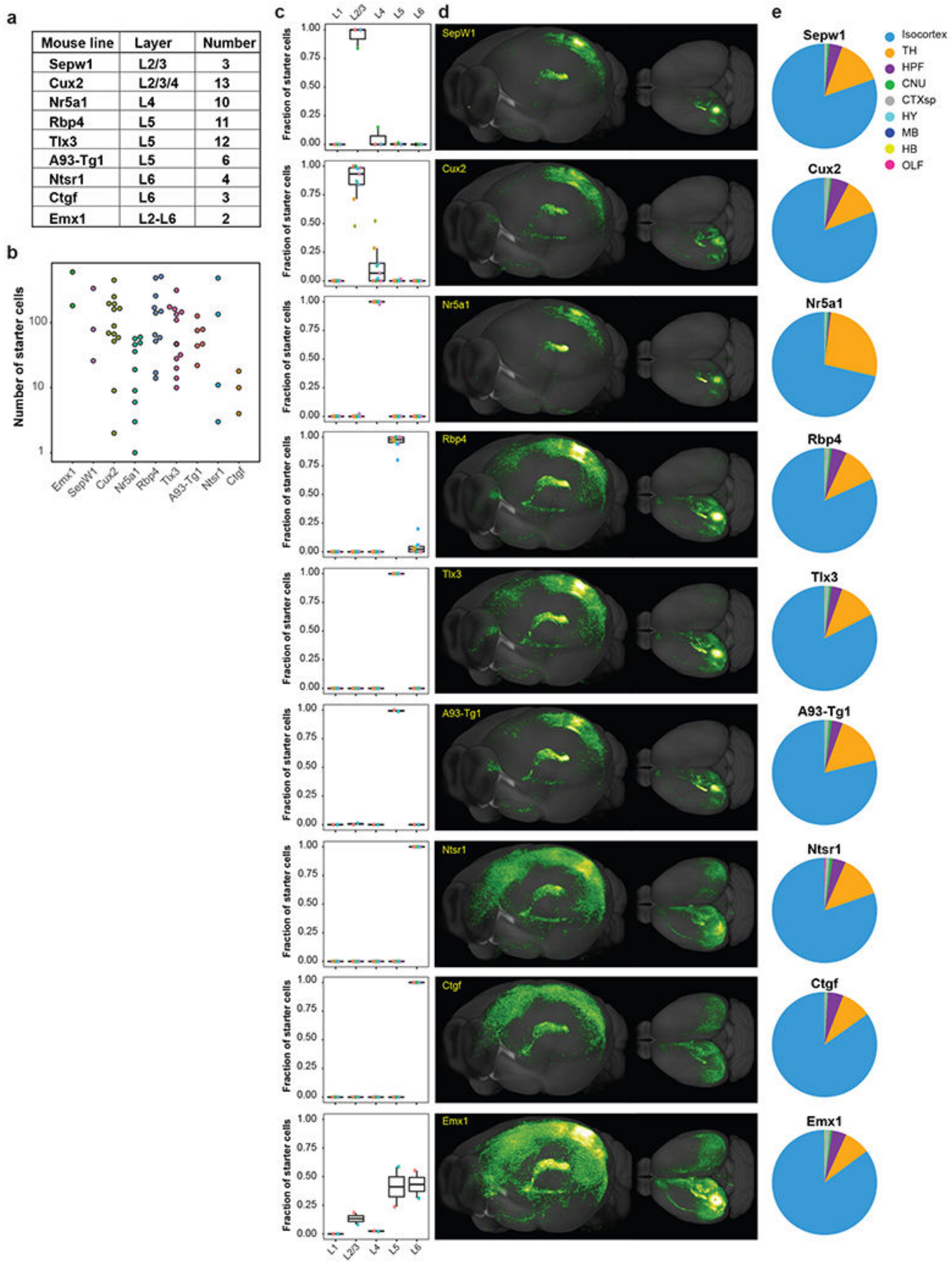

Extended Data Figure 6. Brain-wide input patterns to excitatory neuron subclasses in different layers of the primary visual cortex.

(a-b) Overview of the layer selectivity and number of experiments of each transgenic Cre line (a) and the numbers of starter cells grouped by Cre lines (b) for the 48 experiments in VISp. **(c)** Laminar distribution of starter cells for each Cre line. For each transgenic line, different experiments are indicated by different colors. Box plots show median and interquartile range (IQR). Whiskers show the largest or smallest value no further than 1.5 × IQR from the hinge. The numbers of independent experiments are as follows: Sepw1:

n=3; Cux2: n=13; Nr5a1: n=10; Rbp4: n=11; Tlx3: n=12; A93-Tg1: n=6; Ntsr1: n=4; Ctfg: n=3; Emx1: n=2. **(d)** Representative 3D visualization of brain-wide inputs to neurons in different layers of VISp. **(e)** Brain-wide input patterns of major brain structures to different layer-specific excitatory neuron subclasses labeled by Cre lines.

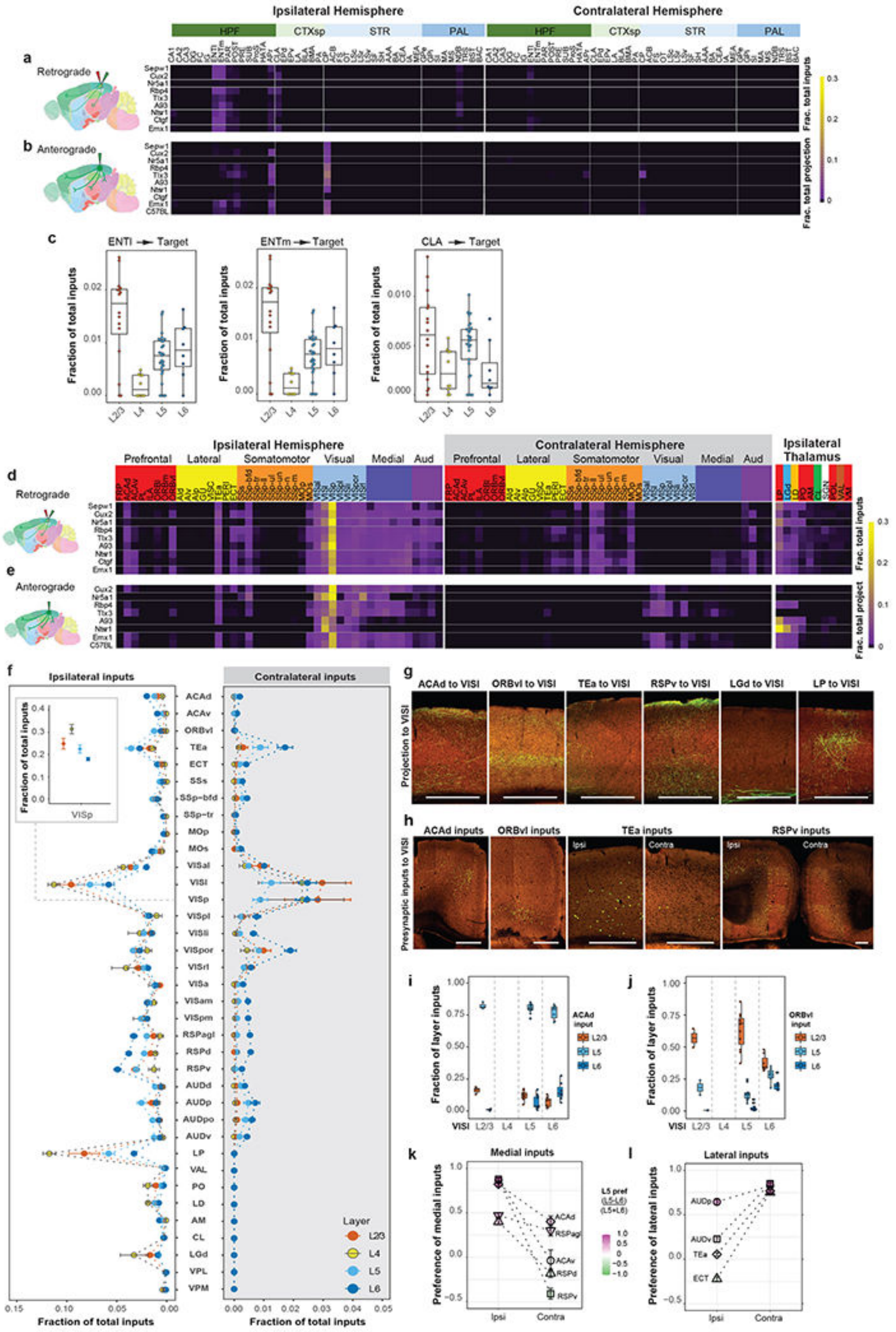

Extended Data Figure 7. Comparison of subcortical inputs to excitatory neurons in different layers of VISp and brain-wide input patterns to excitatory neuron subclasses in VISl.

(**a**) Connectivity matrix showing presynaptic inputs from the ipsilateral and contralateral HPF, CTXsp, STR, and PAL to excitatory neurons in different layers of VISp. Each row of the matrix represents the mean per structure fraction of total input signals for experiments in each Cre line. Rows are organized based on layer-specific distribution of the starter cells. Brain regions are ordered by ontology order in the Allen CCFv3. **(b)** Connectivity matrix showing normalized projections from VISp to the brain regions shown in (a). Anterograde tracing experiments (Supplementary Table 4) from the Cre mouse lines used in (a) and C57BL/6J were included, and rows represent the mean per structure fraction of total projection signals for experiments in each mouse line. **(c)** Comparison of ENTl, ENTm, and CLA inputs to excitatory neurons in different layers of VISp. Box plots show median and interquartile range (IQR). Whiskers show the largest or smallest value no further than 1.5 × IQR from the hinge (same below). The numbers of independent experiments are as follows: L2/3: n=16; L4: n=10; L5: n=29; L6: n=7. **(d)** Connectivity matrix showing normalized inputs from the ipsilateral and contralateral isocortex, and ipsilateral thalamus to excitatory neurons in different layers of VISl. Each row of the matrix represents the mean per structure fraction of total input signals for experiments in each Cre line. Rows are organized based on layer-specific distribution of the starter cells. The cortical areas are ordered first by module membership (color coded) then by ontology order in the Allen CCFv3. The ten thalamic nuclei are ordered based on the strength of inputs, and are color coded by the thalamocortical projection classes (blue: core, green: intralaminar, brown: matrix-focal, and red: matrix-multiareal). **(e)** Connectivity matrix showing normalized axon projections from VISl to the ipsilateral and contralateral isocortex, and ipsilateral thalamus shown in (d). Anterograde tracing experiments (Supplementary Table 5) from the Cre mouse lines used in (d) and C57BL/6J were included, and rows represent the mean per structure fraction of total projection signals for experiments in each mouse line. **(f)** Comparison of inputs from ipsilateral and contralateral cortical areas and thalamic nuclei to excitatory neurons in different layers of VISl. The inset shows fraction of inputs from VISp to excitatory neurons in different layers of VISl. Data are shown as mean ± s.e.m. The numbers of independent experiments are as follows: L2/3: n=5; L4: n=4; L5: n=11; L6: n=8. **(g-h)** Representative STPT images showing laminar termination patterns of axon projections in VISl from higher-order association cortical areas and thalamic nuclei (g) and laminar distribution patterns of presynaptic input cells in the cortical areas that project to VISl (h). Ipsi, ipsilateral hemisphere. Contra, contralateral hemisphere. **(i-j)** Quantification of laminar distribution of inputs from ACAd (i, numbers of independent experiments: L2/3: n=3; L5: n=10; L6: n=7) and ORBvl (j, numbers of independent experiments: L2/3: n=2; L5: n=11; L6: n=7) to excitatory neurons in different layers of VISl. The fraction of layer inputs is calculated as the fraction of the total input signals in a given source area across layers. **(k-l)** Comparison of L5 and L6 preference for medial (k) or lateral (l) source cortical areas in the ipsilateral and contralateral hemispheres sending presynaptic inputs to VISl. The preference score for a given cortical area is calculated as (L5 input - L6 input) / (L5 input + L6 input). Each source cortical area was colored according to its preference score. Data are shown as mean ± s.e.m. The numbers of independent experiments included are as follows: ACAd (Ipsi): n=35; ACAv (Ipsi): n=26; RSPd (Ipsi): n=40; RSPv (Ipsi): n=43, RSPagl (Ipsi): n=36, AUDp (Ipsi): n=39, AUDv (Ipsi): n=30; TEa (Ipsi): n=42, ECT (Ipsi): n=30, ACAd (Contra): n=8; ACAv (Contra): n=4; RSPd (Contra): n=14; RSPv (Contra): n=10, RSPagl (Contra): n=13, AUDp (Contra): n=17, AUDv (Contra): n=13; TEa (Contra): n=26, ECT (Contra): n=14. Scale bars, 500 μm. We also find generally consistent input patterns to excitatory neurons in different layers of other HVAs as of VISp and VISl, though due to smaller number of experiments in each layer of each region (Figure 2a) we do not provide quantitative analysis here.

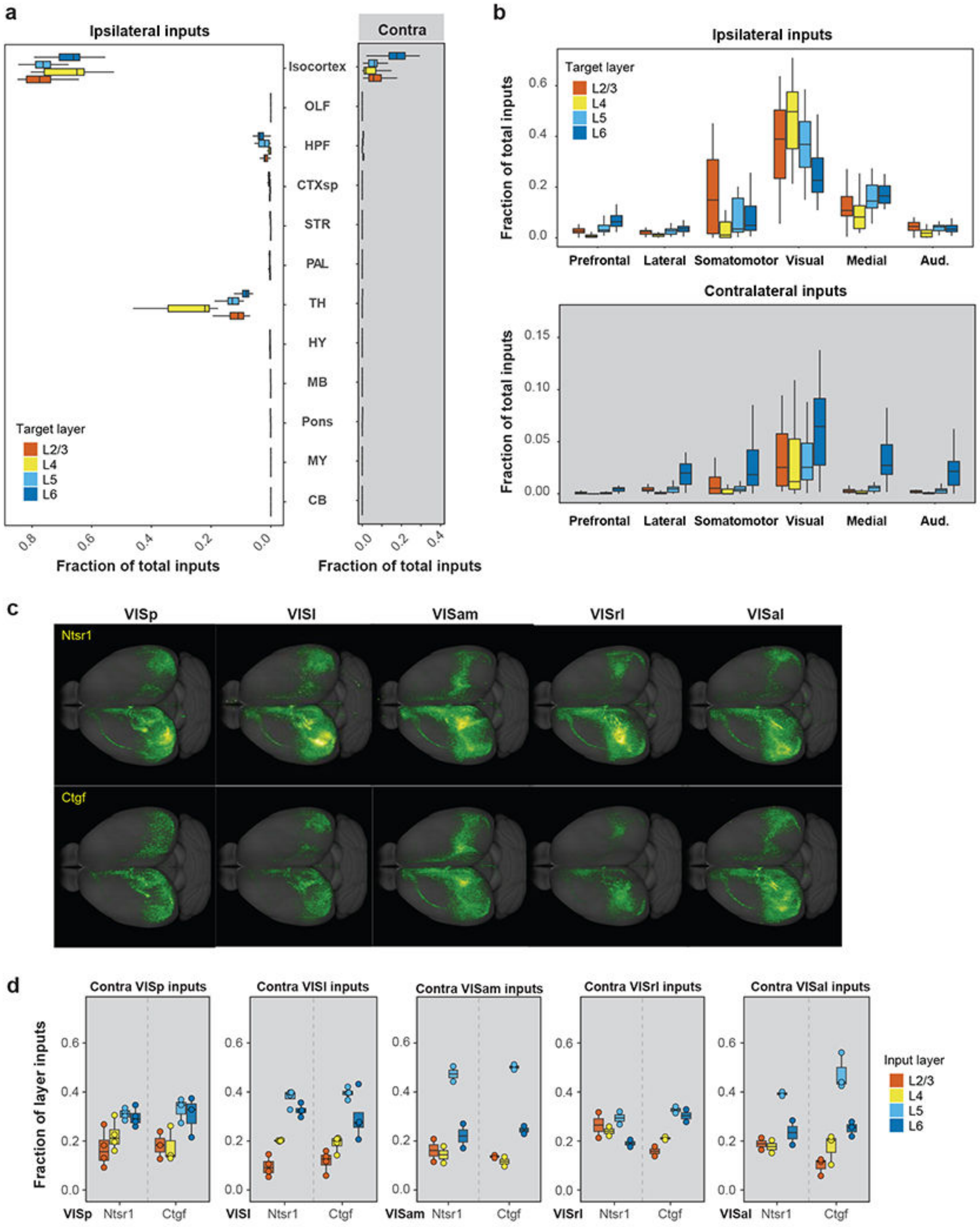

Extended Data Figure 8. Comparison of contralateral cortical inputs to excitatory neuron subclasses in different layers of visual areas.

(a) Comparison between ipsilateral (left) and contralateral (right) brain-wide inputs to excitatory neuron subclasses with starter cells restricted to either L2/3, L4, L5 or L6 of visual areas. A total of 89 experiments with starter cells restricted in a single layer were identified, and the target areas included both VISp and HVAs. **(b)** Comparison between ipsilateral (top) and contralateral (bottom) isocortical inputs for each cortical module to excitatory neuron subclasses with starter cells restricted to either L2/3 (n=20 numbers of independent experiments), L4 (n=18 numbers of independent experiments), L5 (n=25 numbers of independent experiments) or L6 (n=27 numbers of independent experiments) of visual areas. **(c)** Representative top-down view of inputs to Ntsr1 and Ctgf Cre line-labeled L6 and L6b cell types in visual areas. **(d)** Laminar distribution of presynaptic inputs from the homotypic contralateral areas to Ntsr1 and Ctgf Cre line-labeled neurons in visual areas shown in (c). The fraction of layer inputs is calculated as the fraction of the total input signals in a given source area across layers. L1 is excluded from the analysis due to overall lack of signal in this layer. Box plots show median and interquartile range (IQR). Whiskers show the largest or smallest value no further than 1.5 × IQR from the hinge. The numbers of independent experiments are as follows: Ntsr1 in VISp: n=4; Ctgf in VISp: n=3; Ntsr1 in VISl: n=4; Ctgf in VISl: n=4; Ntsr1 in VISam: n=2; Ctgf in VISam: n=2; Ntsr1 in VISrl: n=2; Ctgf in VISrl: n=2; Ntsr1 in VISal: n=2; Ctgf in VISal: n=3.

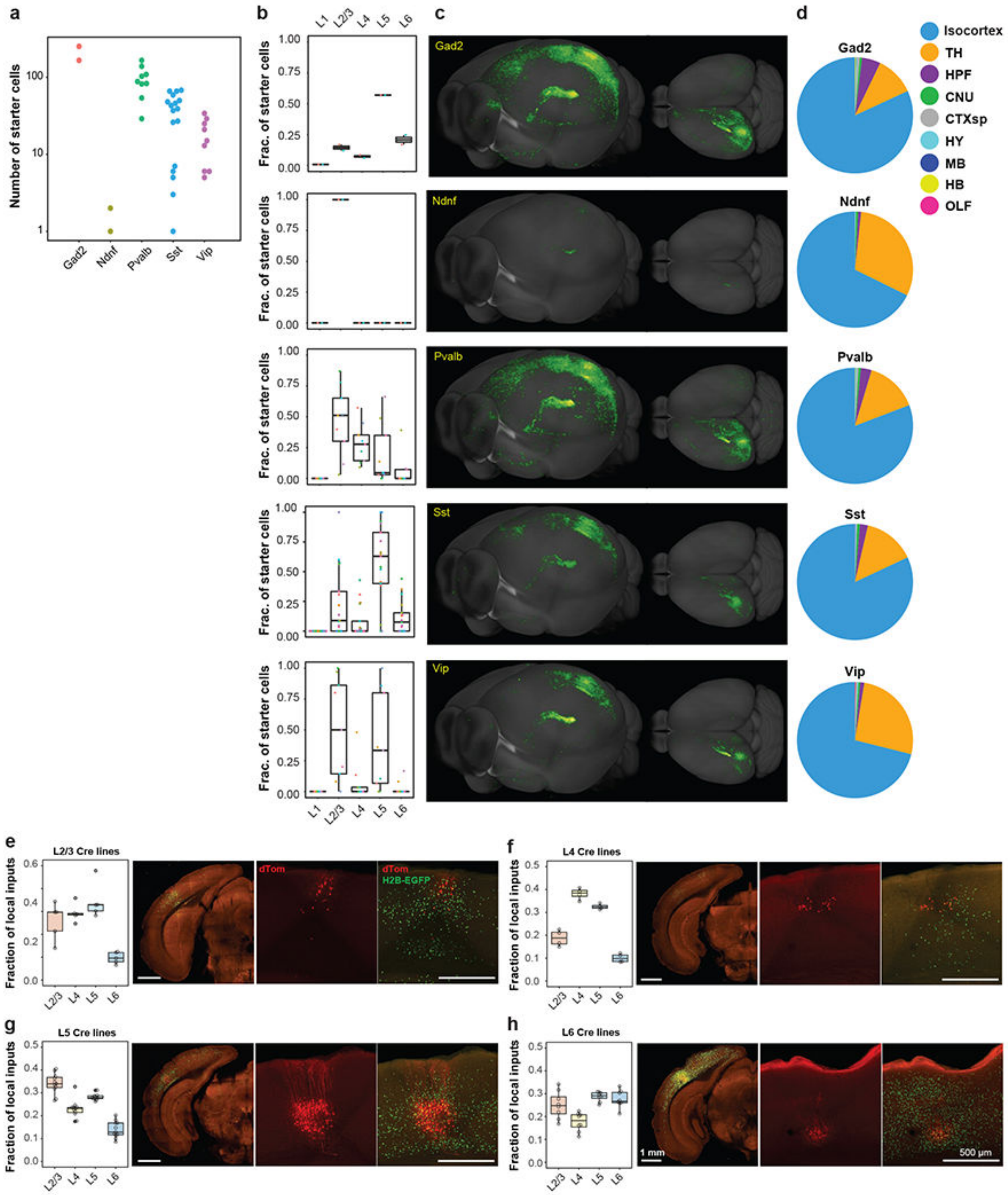

Extended Data Figure 9. Analysis of brain-wide input patterns to interneuron subclasses in VISp, and comparison of local inputs to excitatory neurons in different layers of VISl.

(a) Summary of the numbers of starter cells for each interneuron subclass. Each dot represents one individual experiment. **(b)** Laminar distribution of starter cells for each interneuron subclass. For each transgenic line, different experiments are indicated by different colors. Box plots show median and interquartile range (IQR). Whiskers show the largest or smallest value no further than 1.5 × IQR from the hinge (same below). The number of independent experiments included are as follows: Gad2: n=2; Ndnf:

n=2; Pvalb: n=9; Sst: n=17; Vip: n=9. **(c)** Representative 3D visualization of brain-wide inputs to interneuron subclasses in VISp. **(d)** Overview of brain-wide inputs to different interneuron subclasses. **(e-h)** Layer-specific inputs of ipsilateral VISl to excitatory neurons in L2/3 (e, n=5 independent experiments), L4 (f, n=4 independent experiments), L5 (g, n=11 independent experiments) and L6 (h, n=8 independent experiments) of VISl and representative images of local VISl inputs. Starter cells are identified by the co-expression of dTomato from the AAV helper virus and nucleus-localized H2B-EGFP from the rabies virus.

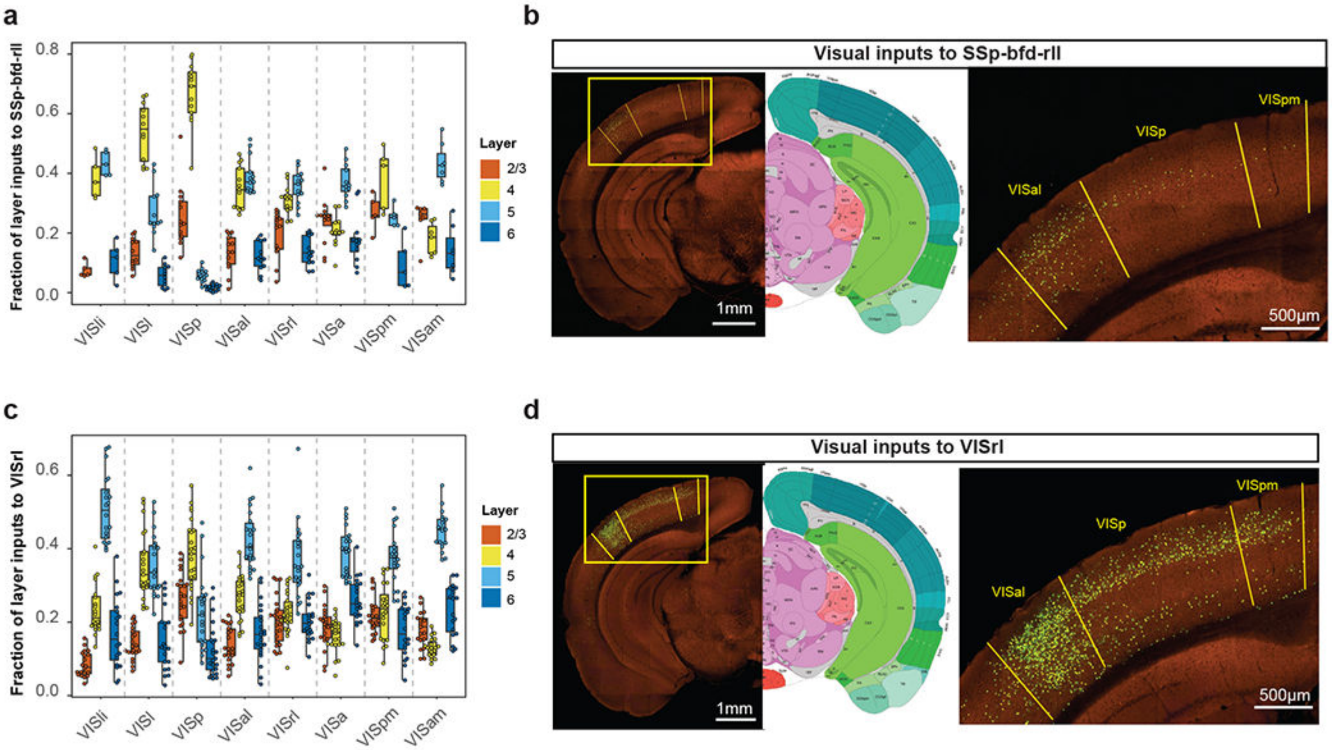

Extended Data Figure 10. Comparison of laminar distribution of visual inputs to SSp-bfd-rll (a-b) and VISrl (c-d).

(a, c) Laminar distribution of inputs from various visual areas to SSp-bfd-rll (a, the numbers of independent experiments are: VISli and VISpm: n=5, VISl and VISa: n=12; VISp, VISal, and VISrl: n=13; VISam: n=7) and VISrl (c, the numbers of independent experiments are: VISli and VISpm: n=20, VISl and VISa: n=21; VISp: n=23; VISal and VISrl: n=22; VISam: n=19). Box plots show median and interquartile range (IQR). Whiskers show the largest or smallest value no further than 1.5 × IQR from the hinge. **(b, d)** Representative images of inputs from VISp, VISpm and VISal to SSp-bfd-rll (b) and VISrl (d).

Supplementary Material

Refer to Web version on PubMed Central for supplementary material.

Authors

Shenqin Yao[1,*], Quanxin Wang[1], Karla E. Hirokawa[1,†], Benjamin Ouellette[1], Ruweida Ahmed[1], Jasmin Bomben[1], Krissy Brouner[1], Linzy Casal[1], Shiella Caldejon[1], Andy Cho[1], Nadezhda I. Dotson[1], Tanya L. Daigle[1], Tom Egdorf[1], Rachel Enstrom[1], Amanda Gary[1], Emily Gelfand[1], Melissa Gorham[1], Fiona Griffin[1], Hong Gu[1], Nicole Hancock[1], Robert Howard[1], Leonard Kuan[1], Sophie Lambert[1], Eric Kenji Lee[1], Jennifer Luviano[1], Kyla Mace[1], Michelle Maxwell[1], Marty T. Mortrud[1], Maitham Naeemi[1], Chelsea Nayan[1], Nhan-Kiet Ngo[1], Thuyanh Nguyen[1], Kat North[1,†], Shea Ransford[1], Augustin Ruiz[1], Sam Seid[1], Jackie Swapp[1], Michael J Taormina[1], Wayne Wakeman[1], Thomas Zhou[1], Philip R. Nicovich[1,†], Ali Williford[1], Lydia Potekhina[1], Medea McGraw[1], Lydia Ng[1], Peter A. Groblewski[1], Bosiljka Tasic[1], Stefan Mihalas[1], Julie A Harris[1,†], Ali Cetin[1,#], Hongkui Zeng[1,*]

Affiliations

[1]Allen Institute for Brain Science, Seattle, WA 98109, USA

Acknowledgments

We are grateful to the Transgenic Colony Management, Neurosurgery & Behavior, Lab Animal Services, Molecular Genetics, Imaging, Histology, Technology, and Project Management teams at the Allen Institute for technical and management support. We thank Thomas R. Reardon, Andrew J. Murray and Ian Wickersham for providing cell lines and plasmids for the establishment of rabies virus production at the Allen Institute. This work was supported by the Allen Institute for Brain Science and by the National Institute of Mental Health (NIMH) of the National Institutes of Health (NIH) under award number U19MH114830 to H.Z. The funders had no role in study design, data collection and analysis, decision to publish or preparation of the manuscript. The content is solely the responsibility of the authors and does not necessarily represent the official views of NIH and its subsidiary institutes. We thank the Allen Institute founder, Paul G. Allen, for his vision, encouragement, and support.

Data Availability

Plasmids for the generation of recombinant viruses will be deposited in Addgene. All anterograde tracing data (including high-resolution STPT images, and informatically processed axonal projections across brain structures) are available through the Allen Mouse Brain Connectivity Atlas portal (http://connectivity.brain-map.org/). A link for each anterograde tracing experiment is provided in Supplementary Tables 4 and 5. Original images for trans-synaptic rabies viral tracing will be or already are available through the Brain Image Library (BIL) (https://www.brainimagelibrary.org/). A link for each trans-synaptic rabies tracing experiment that has been deposited in BIL is provided in Supplementary Table 2. Normalized presynaptic input volumes as fractions of total inputs across the brain for all rabies virus tracing experiments and preliminary retrograde labeling data from initial informatic quantification are listed in Supplementary Table 3.

References:

1. Callaway EM Transneuronal circuit tracing with neurotropic viruses. Current opinion in neurobiology 18, 617–623, doi:10.1016/j.conb.2009.03.007 (2008). [PubMed: 19349161]
2. Callaway EM & Luo L Monosynaptic Circuit Tracing with Glycoprotein-Deleted Rabies Viruses. J Neurosci 35, 8979–8985, doi:10.1523/JNEUROSCI.0409-15.2015 (2015). [PubMed: 26085623]

3. Beier KT et al. Rabies screen reveals GPe control of cocaine-triggered plasticity. Nature 549, 345–350, doi:10.1038/nature23888 (2017). [PubMed: 28902833]

4. Kim EJ, Jacobs MW, Ito-Cole T & Callaway EM Improved Monosynaptic Neural Circuit Tracing Using Engineered Rabies Virus Glycoproteins. Cell reports 15, 692–699, doi:10.1016/j.celrep.2016.03.067 (2016). [PubMed: 27149846]

5. Lo L & Anderson DJ A Cre-dependent, anterograde transsynaptic viral tracer for mapping output pathways of genetically marked neurons. Neuron 72, 938–950, doi:10.1016/j.neuron.2011.12.002 (2011). [PubMed: 22196330]

6. Lo L et al. Connectional architecture of a mouse hypothalamic circuit node controlling social behavior. Proc Natl Acad Sci U S A 116, 7503–7512, doi:10.1073/pnas.1817503116 (2019). [PubMed: 30898882]

7. Miyamichi K et al. Cortical representations of olfactory input by trans-synaptic tracing. Nature 472, 191–196, doi:10.1038/nature09714 (2011). [PubMed: 21179085]

8. Miyamichi K et al. Dissecting local circuits: parvalbumin interneurons underlie broad feedback control of olfactory bulb output. Neuron 80, 1232–1245, doi:10.1016/j.neuron.2013.08.027 (2013). [PubMed: 24239125]

9. Osakada F et al. New rabies virus variants for monitoring and manipulating activity and gene expression in defined neural circuits. Neuron 71, 617–631, doi:10.1016/j.neuron.2011.07.005 (2011). [PubMed: 21867879]

10. Wall NR, Wickersham IR, Cetin A, De La Parra M & Callaway EM Monosynaptic circuit tracing in vivo through Cre-dependent targeting and complementation of modified rabies virus. Proceedings of the National Academy of Sciences of the United States of America 107, 21848–21853, doi:10.1073/pnas.1011756107 (2010). [PubMed: 21115815]

11. Watabe-Uchida M, Zhu L, Ogawa SK, Vamanrao A & Uchida N Whole-brain mapping of direct inputs to midbrain dopamine neurons. Neuron 74, 858–873, doi:10.1016/j.neuron.2012.03.017 (2012). [PubMed: 22681690]

12. Weible AP et al. Transgenic targeting of recombinant rabies virus reveals monosynaptic connectivity of specific neurons. J Neurosci 30, 16509–16513, doi:10.1523/JNEUROSCI.2442-10.2010 (2010). [PubMed: 21147990]

13. Weissbourd B et al. Presynaptic partners of dorsal raphe serotonergic and GABAergic neurons. Neuron 83, 645–662, doi:10.1016/j.neuron.2014.06.024 (2014). [PubMed: 25102560]

14. Wickersham IR, Finke S, Conzelmann KK & Callaway EM Retrograde neuronal tracing with a deletion-mutant rabies virus. Nature methods 4, 47–49, doi:10.1038/nmeth999 (2007). [PubMed: 17179932]

15. Wickersham IR et al. Monosynaptic restriction of transsynaptic tracing from single, genetically targeted neurons. Neuron 53, 639–647, doi:10.1016/j.neuron.2007.01.033 (2007). [PubMed: 17329205]

16. Reardon TR et al. Rabies Virus CVS-N2c(DeltaG) Strain Enhances Retrograde Synaptic Transfer and Neuronal Viability. Neuron 89, 711–724, doi:10.1016/j.neuron.2016.01.004 (2016). [PubMed: 26804990]

17. Chatterjee S et al. Nontoxic, double-deletion-mutant rabies viral vectors for retrograde targeting of projection neurons. Nature neuroscience 21, 638–646, doi:10.1038/s41593-018-0091-7 (2018). [PubMed: 29507411]

18. Ciabatti E, Gonzalez-Rueda A, Mariotti L, Morgese F & Tripodi M Life-Long Genetic and Functional Access to Neural Circuits Using Self-Inactivating Rabies Virus. Cell 170, 382–392 e314, doi:10.1016/j.cell.2017.06.014 (2017). [PubMed: 28689641]

19. Hafner G et al. Mapping Brain-Wide Afferent Inputs of Parvalbumin-Expressing GABAergic Neurons in Barrel Cortex Reveals Local and Long-Range Circuit Motifs. Cell Rep 28, 3450–3461 e3458, doi:10.1016/j.celrep.2019.08.064 (2019). [PubMed: 31553913]

20. Harris JA et al. Hierarchical organization of cortical and thalamic connectivity. Nature 575, 195–202, doi:10.1038/s41586-019-1716-z (2019). [PubMed: 31666704]

21. Oh SW et al. A mesoscale connectome of the mouse brain. Nature 508, 207–214, doi:10.1038/nature13186 (2014). [PubMed: 24695228]

22. Wang Q et al. The Allen Mouse Brain Common Coordinate Framework: A 3D Reference Atlas. Cell 181, 936–953 e920, doi:10.1016/j.cell.2020.04.007 (2020). [PubMed: 32386544]
23. Kuan L et al. Neuroinformatics of the Allen Mouse Brain Connectivity Atlas. Methods (San Diego, Calif 73, 4–17, doi:10.1016/j.ymeth.2014.12.013 (2015). [PubMed: 25536338]
24. Wang Q & Burkhalter A Area map of mouse visual cortex. The Journal of comparative neurology 502, 339–357, doi:10.1002/cne.21286 (2007). [PubMed: 17366604]
25. Zhuang J et al. An extended retinotopic map of mouse cortex. eLife 6, doi:10.7554/eLife.18372 (2017).
26. Garrett ME, Nauhaus I, Marshel JH & Callaway EM Topography and areal organization of mouse visual cortex. J Neurosci 34, 12587–12600, doi:10.1523/JNEUROSCI.1124-14.2014 (2014). [PubMed: 25209296]
27. Gamanut R et al. The Mouse Cortical Connectome, Characterized by an Ultra-Dense Cortical Graph, Maintains Specificity by Distinct Connectivity Profiles. Neuron 97, 698–715 e610, doi:10.1016/j.neuron.2017.12.037 (2018). [PubMed: 29420935]
28. Wang Q, Sporns O & Burkhalter A Network analysis of corticocortical connections reveals ventral and dorsal processing streams in mouse visual cortex. J Neurosci 32, 4386–4399, doi:10.1523/JNEUROSCI.6063-11.2012 (2012). [PubMed: 22457489]
29. Felleman DJ & Van Essen DC Distributed hierarchical processing in the primate cerebral cortex. Cereb Cortex 1, 1–47, doi:10.1093/cercor/1.1.1 (1991). [PubMed: 1822724]
30. Markov NT et al. Anatomy of hierarchy: feedforward and feedback pathways in macaque visual cortex. The Journal of comparative neurology 522, 225–259, doi:10.1002/cne.23458 (2014). [PubMed: 23983048]
31. Tasic B et al. Shared and distinct transcriptomic cell types across neocortical areas. Nature 563, 72–78, doi:10.1038/s41586-018-0654-5 (2018). [PubMed: 30382198]
32. Kohara K et al. Cell type-specific genetic and optogenetic tools reveal hippocampal CA2 circuits. Nature neuroscience 17, 269–279, doi:10.1038/nn.3614 (2014). [PubMed: 24336151]
33. Ahrlund-Richter S et al. A whole-brain atlas of monosynaptic input targeting four different cell types in the medial prefrontal cortex of the mouse. Nat Neurosci 22, 657–668, doi:10.1038/s41593-019-0354-y (2019). [PubMed: 30886408]
34. Huppe-Gourgues F, Jegouic K & Vaucher E Topographic Organization of Cholinergic Innervation From the Basal Forebrain to the Visual Cortex in the Rat. Front Neural Circuits 12, 19, doi:10.3389/fncir.2018.00019 (2018). [PubMed: 29662442]
35. Li X et al. Generation of a whole-brain atlas for the cholinergic system and mesoscopic projectome analysis of basal forebrain cholinergic neurons. Proc Natl Acad Sci U S A 115, 415–420, doi:10.1073/pnas.1703601115 (2018). [PubMed: 29259118]
36. Bari BA, Chokshi V & Schmidt K Locus coeruleus-norepinephrine: basic functions and insights into Parkinson’s disease. Neural Regen Res 15, 1006–1013, doi:10.4103/1673-5374.270297 (2020). [PubMed: 31823870]
37. Schwarz LA et al. Viral-genetic tracing of the input-output organization of a central noradrenaline circuit. Nature 524, 88–92, doi:10.1038/nature14600 (2015). [PubMed: 26131933]
38. Ren J et al. Single-cell transcriptomes and whole-brain projections of serotonin neurons in the mouse dorsal and median raphe nuclei. eLife 8, doi:10.7554/eLife.49424 (2019).
39. Beltramo R & Scanziani M A collicular visual cortex: Neocortical space for an ancient midbrain visual structure. Science 363, 64–69, doi:10.1126/science.aau7052 (2019). [PubMed: 30606842]
40. Antonini A, Fagiolini M & Stryker MP Anatomical correlates of functional plasticity in mouse visual cortex. J Neurosci 19, 4388–4406 (1999). [PubMed: 10341241]
41. Humphrey AL, Sur M, Uhlrich DJ & Sherman SM Projection patterns of individual X- and Y-cell axons from the lateral geniculate nucleus to cortical area 17 in the cat. J Comp Neurol 233, 159–189, doi:10.1002/cne.902330203 (1985). [PubMed: 3973100]
42. LeVay S & Gilbert CD Laminar patterns of geniculocortical projection in the cat. Brain Res 113, 1–19, doi:10.1016/0006-8993(76)90002-0 (1976). [PubMed: 953720]
43. Ji XY et al. Thalamocortical Innervation Pattern in Mouse Auditory and Visual Cortex: Laminar and Cell-Type Specificity. Cereb Cortex 26, 2612–2625, doi:10.1093/cercor/bhv099 (2016). [PubMed: 25979090]

44. Cruikshank SJ, Urabe H, Nurmikko AV & Connors BW Pathway-specific feedforward circuits between thalamus and neocortex revealed by selective optical stimulation of axons. Neuron 65, 230–245, doi:10.1016/j.neuron.2009.12.025 (2010). [PubMed: 20152129]
45. Velez-Fort M et al. The stimulus selectivity and connectivity of layer six principal cells reveals cortical microcircuits underlying visual processing. Neuron 83, 1431–1443, doi:10.1016/j.neuron.2014.08.001 (2014). [PubMed: 25175879]
46. Velez-Fort M et al. A Circuit for Integration of Head- and Visual-Motion Signals in Layer 6 of Mouse Primary Visual Cortex. Neuron 98, 179–191 e176, doi:10.1016/j.neuron.2018.02.023 (2018). [PubMed: 29551490]
47. Xu X & Callaway EM Laminar specificity of functional input to distinct types of inhibitory cortical neurons. J Neurosci 29, 70–85, doi:10.1523/JNEUROSCI.4104-08.2009 (2009). [PubMed: 19129386]
48. DeNardo LA, Berns DS, DeLoach K & Luo L Connectivity of mouse somatosensory and prefrontal cortex examined with trans-synaptic tracing. Nat Neurosci 18, 1687–1697, doi:10.1038/nn.4131 (2015). [PubMed: 26457553]
49. Munoz-Castaneda R et al. Cellular anatomy of the mouse primary motor cortex. Nature 598, 159–166, doi:10.1038/s41586-021-03970-w (2021). [PubMed: 34616071]
50. Sun Q et al. A whole-brain map of long-range inputs to GABAergic interneurons in the mouse medial prefrontal cortex. Nat Neurosci 22, 1357–1370, doi:10.1038/s41593-019-0429-9 (2019). [PubMed: 31285615]
51. Kim EJ, Juavinett AL, Kyubwa EM, Jacobs MW & Callaway EM Three Types of Cortical Layer 5 Neurons That Differ in Brain-wide Connectivity and Function. Neuron 88, 1253–1267, doi:10.1016/j.neuron.2015.11.002 (2015). [PubMed: 26671462]
52. Liang Y et al. A Distinct Population of L6 Neurons in Mouse V1 Mediate Cross-Callosal Communication. Cereb Cortex 31, 4259–4273, doi:10.1093/cercor/bhab084 (2021). [PubMed: 33987642]
53. Liu YJ et al. Tracing inputs to inhibitory or excitatory neurons of mouse and cat visual cortex with a targeted rabies virus. Curr Biol 23, 1746–1755, doi:10.1016/j.cub.2013.07.033 (2013). [PubMed: 23993841]
54. Brown APY et al. Analysis of segmentation ontology reveals the similarities and differences in connectivity onto L2/3 neurons in mouse V1. Sci Rep 11, 4983, doi:10.1038/s41598-021-82353-7 (2021). [PubMed: 33654118]
55. Kim EJ et al. Extraction of Distinct Neuronal Cell Types from within a Genetically Continuous Population. Neuron 107, 274–282 e276, doi:10.1016/j.neuron.2020.04.018 (2020). [PubMed: 32396852]
56. Peng H et al. Morphological diversity of single neurons in molecularly defined cell types. Nature 598, 174–181, doi:10.1038/s41586-021-03941-1 (2021). [PubMed: 34616072]
57. D’Souza RD et al. Hierarchical and nonhierarchical features of the mouse visual cortical network. Nat Commun 13, 503, doi:10.1038/s41467-022-28035-y (2022). [PubMed: 35082302]
58. Siegle JH et al. Survey of spiking in the mouse visual system reveals functional hierarchy. Nature 592, 86–92, doi:10.1038/s41586-020-03171-x (2021). [PubMed: 33473216]
59. Masse IO, Ross S, Bronchti G & Boire D Asymmetric Direct Reciprocal Connections Between Primary Visual and Somatosensory Cortices of the Mouse. Cereb Cortex 27, 4361–4378, doi:10.1093/cercor/bhw239 (2017). [PubMed: 27522075]
60. Han X, Vermaercke B & Bonin V Diversity of spatiotemporal coding reveals specialized visual processing streams in the mouse cortex. Nat Commun 13, 3249, doi:10.1038/s41467-022-29656-z (2022). [PubMed: 35668056]

Methods-only references:

61. Gorski JA et al. Cortical excitatory neurons and glia, but not GABAergic neurons, are produced in the Emx1-expressing lineage. J Neurosci 22, 6309–6314, doi:20026564 (2002). [PubMed: 12151506]

62. Franco SJ et al. Fate-restricted neural progenitors in the mammalian cerebral cortex. Science (New York, N.Y 337, 746–749, doi:10.1126/science.1223616 (2012). [PubMed: 22879516]
63. Dhillon H et al. Leptin directly activates SF1 neurons in the VMH, and this action by leptin is required for normal body-weight homeostasis. Neuron 49, 191–203, doi:10.1016/j.neuron.2005.12.021 (2006). [PubMed: 16423694]
64. Gerfen CR, Paletzki R & Heintz N GENSAT BAC cre-recombinase driver lines to study the functional organization of cerebral cortical and basal ganglia circuits. Neuron 80, 1368–1383, doi:10.1016/j.neuron.2013.10.016 (2013). [PubMed: 24360541]
65. Daigle TL et al. A Suite of Transgenic Driver and Reporter Mouse Lines with Enhanced Brain-Cell-Type Targeting and Functionality. Cell 174, 465–480 e422, doi:10.1016/j.cell.2018.06.035 (2018). [PubMed: 30007418]
66. Taniguchi H et al. A resource of Cre driver lines for genetic targeting of GABAergic neurons in cerebral cortex. Neuron 71, 995–1013, doi:10.1016/j.neuron.2011.07.026 (2011). [PubMed: 21943598]
67. Hippenmeyer S et al. A developmental switch in the response of DRG neurons to ETS transcription factor signaling. PLoS biology 3, e159, doi:10.1371/journal.pbio.0030159 (2005). [PubMed: 15836427]
68. Rossi J et al. Melanocortin-4 receptors expressed by cholinergic neurons regulate energy balance and glucose homeostasis. Cell metabolism 13, 195–204, doi:10.1016/j.cmet.2011.01.010 (2011). [PubMed: 21284986]
69. Zawadzka M et al. CNS-resident glial progenitor/stem cells produce Schwann cells as well as oligodendrocytes during repair of CNS demyelination. Cell Stem Cell 6, 578–590, doi:10.1016/j.stem.2010.04.002 (2010). [PubMed: 20569695]
70. Koni PA et al. Conditional vascular cell adhesion molecule 1 deletion in mice: impaired lymphocyte migration to bone marrow. J Exp Med 193, 741–754, doi:10.1084/jem.193.6.741 (2001). [PubMed: 11257140]
71. Octeau JC et al. An Optical Neuron-Astrocyte Proximity Assay at Synaptic Distance Scales. Neuron 98, 49–66 e49, doi:10.1016/j.neuron.2018.03.003 (2018). [PubMed: 29621490]
72. Osakada F & Callaway EM Design and generation of recombinant rabies virus vectors. Nat Protoc 8, 1583–1601, doi:10.1038/nprot.2013.094 (2013). [PubMed: 23887178]
73. Do JP et al. Cell type-specific long-range connections of basal forebrain circuit. Elife 5, doi:10.7554/eLife.13214 (2016).

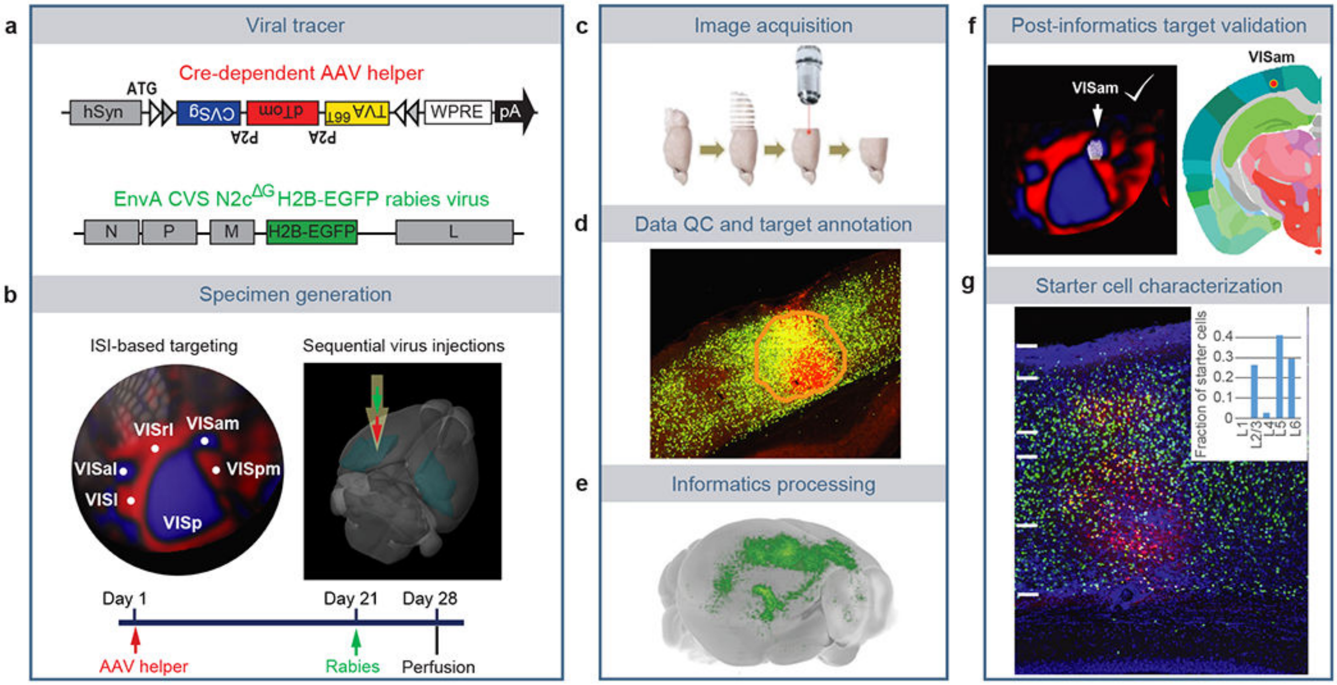

Figure 1. Pipeline identifying monosynaptic inputs to specific neuronal populations in the visual cortex.

(**a**) Viral tools for mapping monosynaptic inputs to Cre-expressing neurons. The tricistronic AAV helper virus conditionally expresses TVA^{66T}, dTomato, and rabies glycoprotein of the CVS N2c strain (CVSg) after Cre-mediated recombination. The EnvA-pseudotyped CVS N2c$^{\Delta G}$ rabies virus expresses histone-EGFP (H2B-EGFP) from the rabies G gene locus in the recombinant rabies virus genome. (**b**) ISI-based targeting, stereotaxic injection, and experimental timeline for virus injections and brain collection. (**c**) Sequential two-photon images were acquired at 100 μm interval and a total of 140 images were obtained for each brain. **(d)** Target sites were annotated by drawing injection polygons based on the expression of dTomato from the AAV helper virus. **(e)** Image series was automatically segmented and registered into the Allen CCFv3. (**f**) Injection site was verified post hoc by overlaying the injection site detected by AAV helper expression with an ISI image, and/or by overlaying the injection centroid to CCFv3. **(g)** Starter cell characterization. Sections around the planned injection site were collected and dTomato signal was enhanced by immunostaining. Starter cells were then detected by co-expression of dTomato and nuclear EGFP, and layer-distribution of the starter cells was analyzed.

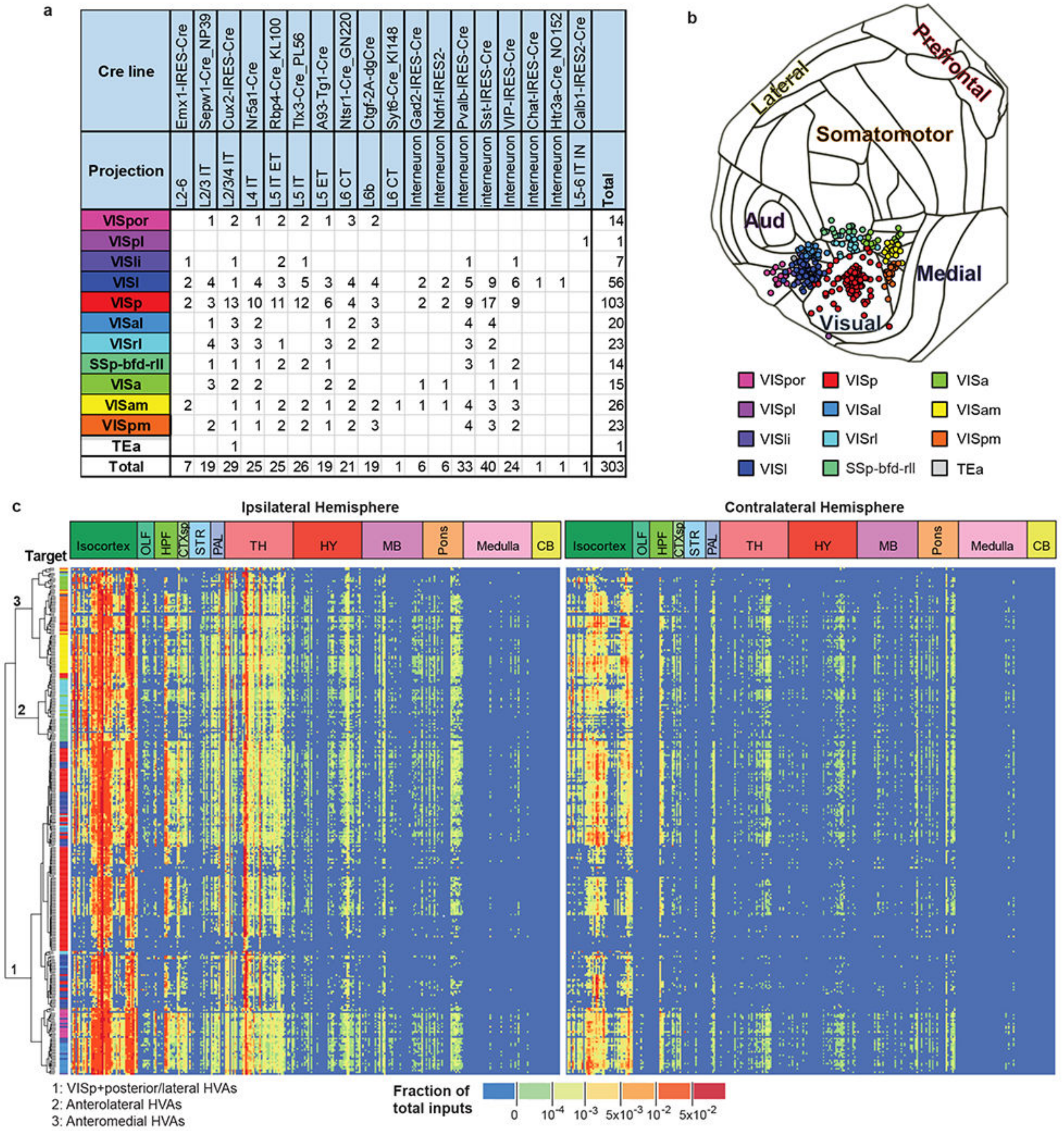

Cre line	Emx1-IRES-Cre	Sepw1-Cre_NP39	Cux2-IRES-Cre	Nr5a1-Cre	Rbp4-Cre_KL100	Tlx3-Cre_PL56	A93-Tg1-Cre	Ntsr1-Cre_GN220	Ctgf-2A-dgCre	Syt6-Cre_KI148	Gad2-IRES-Cre	Ndnf-IRES2-	Pvalb-IRES-Cre	Sst-IRES-Cre	VIP-IRES-Cre	Chat-IRES-Cre	Htr3a-Cre_NO152	Calb1-IRES2-Cre	
Projection	L2-6	L2/3 IT	L2/3/4 IT	L4 IT	L5 IT ET	L5 IT	L5 ET	L6 CT	L6b	L6 CT	Interneuron	Interneuron	Interneuron	interneuron	Interneuron	Interneuron	Interneuron	L5-6 IT IN	**Total**
VISpor		1	2	1	2	2	1	3	2										14
VISpl																		1	1
VISli	1		1		2	1							1		1				7
VISl	2	4	1	4	3	5	3	4	4		2	2	5	9	6	1	1		56
VISp	2	3	13	10	11	12	6	4	3		2	2	9	17	9				103
VISal		1	3	2			1	2	3				4	4					20
VISrl		4	3	3	1		3	2	2				3	2					23
SSp-bfd-rll		1	1	1	2	2	1						3	1	2				14
VISa		3	2	2			2	2			1	1		1	1				15
VISam	2		1	1	2	2	1	2	2	1	1	1	4	3	3				26
VISpm		2	1	1	2	2	1	2	3				4	3	2				23
TEa			1																1
Total	7	19	29	25	25	26	19	21	19	1	6	6	33	40	24	1	1	1	303

Figure 2. Identification of monosynaptic inputs to Cre-labeled neuronal classes in different visual areas.

(a) Summary of Cre mouse lines, target areas, and numbers of the 303 experiments in the visual areas. The injection target areas were verified based on overlay of injection site polygons with ISI images and/or the position of injection site polygons in Allen CCFv3. **(b)** Mapping of each injection centroid in the cortical flat map (with six cortical modules labeled: prefrontal, lateral, somatomotor, visual, medial and auditory). Color indicates different visual areas. Twelve injections were performed into the right hemisphere, the remaining 291 injections were performed into the left hemisphere, and injection site was verified post-hoc. Locations of all injection centroids were plotted onto the CCFv3 cortical flat map, with the right hemisphere injection centroids flipped to their corresponding sites in the left hemisphere for comparative analysis**. (c)** Connectivity matrix showing normalized inputs from the ipsilateral and contralateral hemispheres for all experiments. Each row represents a single experiment. Columns are ordered by 12 major brain divisions; rows are organized according to hierarchical clustering of the input patterns. The input signal per structure was measured by the informatics data pipeline and represented by per structure input signal volume (sum of detected signal in mm^3) after thresholding to minimize false positive signals (see Methods), and then normalized to the total inputs of the whole brain. Value in each cell of the matrix represents the input signal volume in the given brain area as the fraction of total inputs of the brain. Color in the “Target” represents the verified injection target area of the experiment in each row, as color-coded in (b).

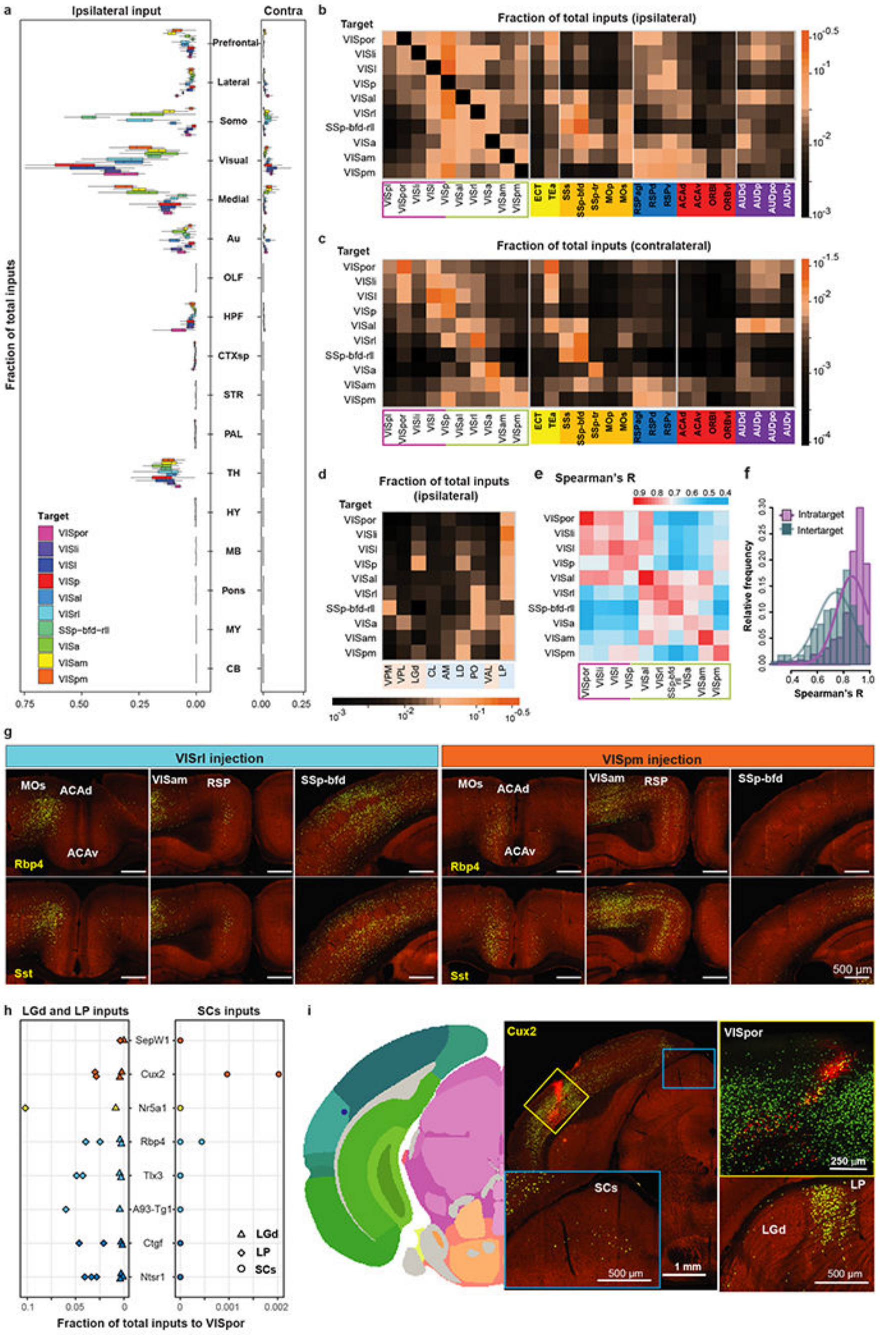

Figure 3. Comparison of brain-wide inputs to neurons in the primary visual cortex and higher visual areas.

(a) Comparison of whole-brain inputs to the visual areas. Inputs from isocortex were divided into six modules. Numbers of independent experiments for each target are in Figure 2a. Box plots show median and interquartile range (IQR). Whiskers show the largest or smallest value no further than 1.5 × IQR from the hinge. Somo, somatomotor. OLF, olfactory areas. HPF, hippocampal formation. CTXsp, cortical subplate. STR, striatum. PAL, pallidum. TH, thalamus. HY, hypothalamus. MB, midbrain. MY, medulla. CB, cerebellum. **(b-d)** Matrices showing inputs to visual area targets from top input areas. Each cell represents the average value of fraction of total inputs from a given input area in all the experiments for a given target. Visual input areas are separated into dorsal and ventral streams and ordered based on their hierarchical organization. Non-visual input cortical areas are grouped by module membership. Input thalamic areas are ordered by previously predicted hierarchical orders[20]. Areas in the sensory-motor cortex related or polymodal association cortex related part of thalamus are highlighted in pink or blue, respectively. **(e)** Matrix showing Spearman's R between experiments within the same target (intra-target, mean of Rs between experiments of different Cre lines) and between experiments across different targets (inter-target, mean of Rs between experiments of same Cre line in different targets). **(f)** Frequency distributions of intra-target and inter-target Spearman's R. A curve was fit to each distribution. **(g)** Comparison of inputs between VISrl (Rbp4: n=1, Sst: n=2) and VISpm (Rbp4: n=2, Sst: n=3). **(h)** Comparison of LGd, LP and SCs inputs to VISpor in 14 experiments. Each symbol represents one experiment. **(i)** Example of a Cux2-IRES-Cre VISpor experiment. Two independent experiments led to similar results. Left: Injection centroid mapped to VISpor in Allen CCFv3. Middle: Brain section containing the injection site and labeling in SCs. Right: Confocal image of the injection site and labeling in LGd and LP.

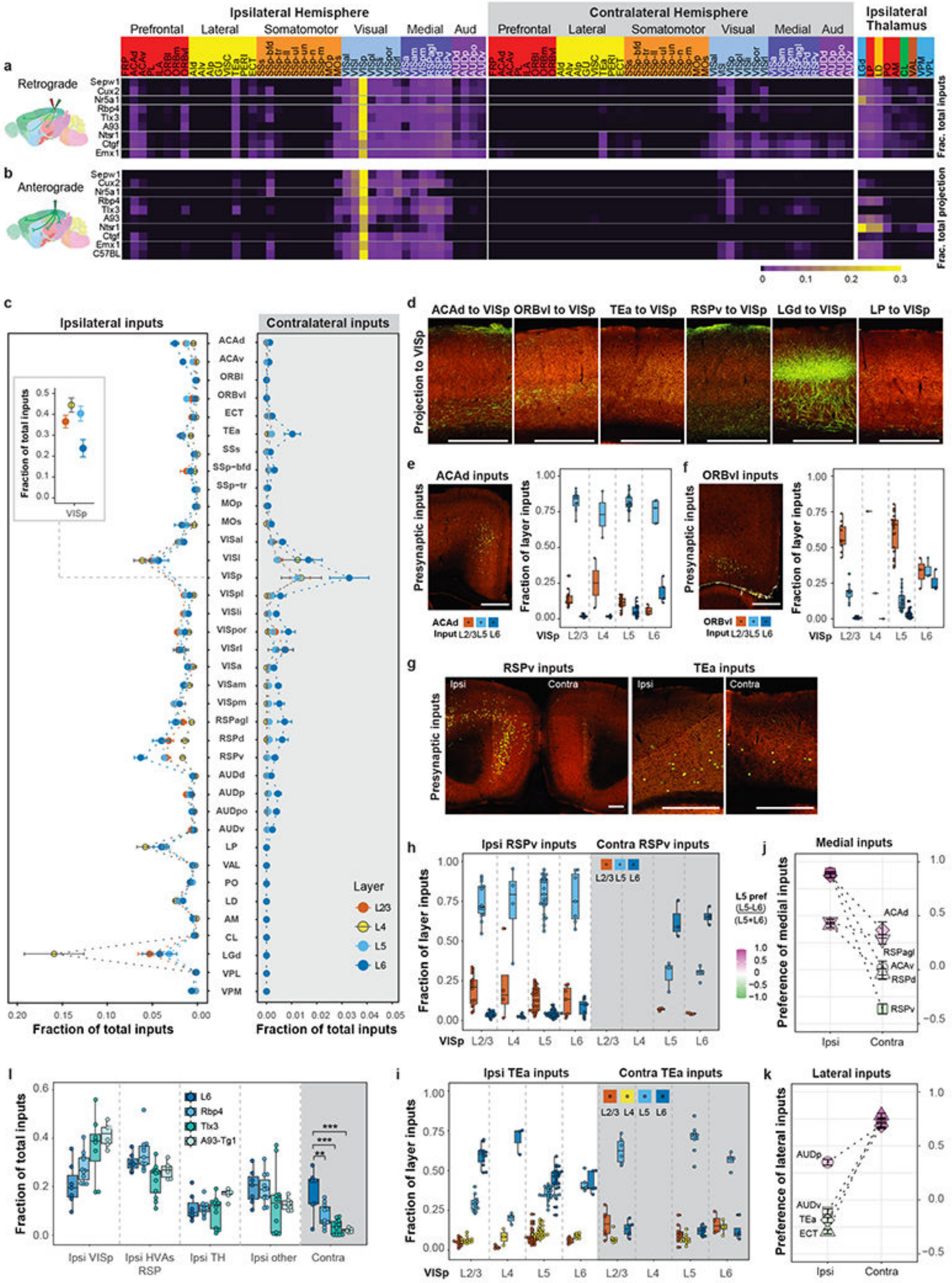

Figure 4. Comparison of brain-wide input patterns to excitatory neuron subclasses in different layers of the primary visual cortex.

(a-b) Matrix showing inputs from the isocortex and thalamus to excitatory neurons in different layers of VISp (a) and matrix showing the reciprocal axonal projections from VISp (b). Each row represents the mean fraction of total input or projection signals per structure in each mouse line. Cortical module memberships and thalamocortical projection classes[20] (blue: core, green: intralaminar, brown: matrix-focal, and red: matrix-multiareal) are color-coded. (**c**) Comparison of inputs to excitatory neurons in different layers of VISp (independent experiments: 16, 10, 29 and 7 for L2/3, L4, L5 and L6, respectively). Data are shown as mean ± s.e.m. The inset shows local VISp inputs. **(d)** Laminar termination patterns of axon projections in VISp from source areas (ACAd: n=3; ORBvl: n=2; TEa, n=1; RSPv: n=2; LGd: n=5; and LP: n=1). **(e-i)** Laminar distribution pattern of input cells in ACAd, ORBvl, RSPv and TEa projecting to excitatory neurons in VISp. The fraction of layer inputs is calculated as the fraction of the total input signals in a given source area across layers. L1 is excluded from the analysis due to overall lack of signal in this layer. Independent experiments: e, 11, 2, 21 and 5 for L2/3, L4, L5 and L6, respectively; f, 10, 1, 24, 3 for L2/3, L4, L5 and L6, respectively; RSPv in g,h: Ipsi: 14, 4, 25, and 7 for L2/3, L4, L5 and L6, respectively; Contra: 3, and 4 for L5 and L6 respectively; TEa in g,i: Ipsi: 12, 3, 24, and 5 for L2/3, L4, L5 and L6, respectively; Contra: 6, 10 and 4 for L2/3, L5 and L6, respectively. **(j-k)** Comparison of L5 and L6 preference for medial (j) or lateral (k) source cortical areas sending inputs to VISp. A preference score for a given cortical area (L5 input - L6 input) / (L5 input + L6 input) shows that ipsilateral inputs to VISp come preferentially from L5 of medial areas and L6 of lateral areas, whereas contralateral inputs to VISp present an opposite bias. Data are shown as mean ± s.e.m. Independent experiments: Ipsi: ACAd: n=56; ACAv: n=40; RSPd: n=73; RSPv: n=78, RSPagl: n=61, AUDp: n=56, AUDv: n=43; TEa: n=65, ECT: n=37; Contra: ACAd: n=9; ACAv: n=8; RSPd: n=17; RSPv: n=12, RSPagl: n=16, AUDp: n=14, AUDv: n=10; TEa: n=27, ECT: n=11. **(l)** Comparison of inputs to L6 and different L5 cell populations in VISp (L6: n=7; Rbp4: n=11; Tlx3: n=12; A93-Tg1: n=6). $^{**}p < 0.01$, $^{***}p < 0.001$. Tukey multiple comparisons of means: L6 vs Rbp4: p=0.0015, L6 vs Tlx3: p=0.000004, L6 vs A93-Tg1: p=0.000015. Box plots show median and interquartile range (IQR). Whiskers show the largest or smallest value no further than 1.5 × IQR from the hinge. Scale bars, 500 μm.

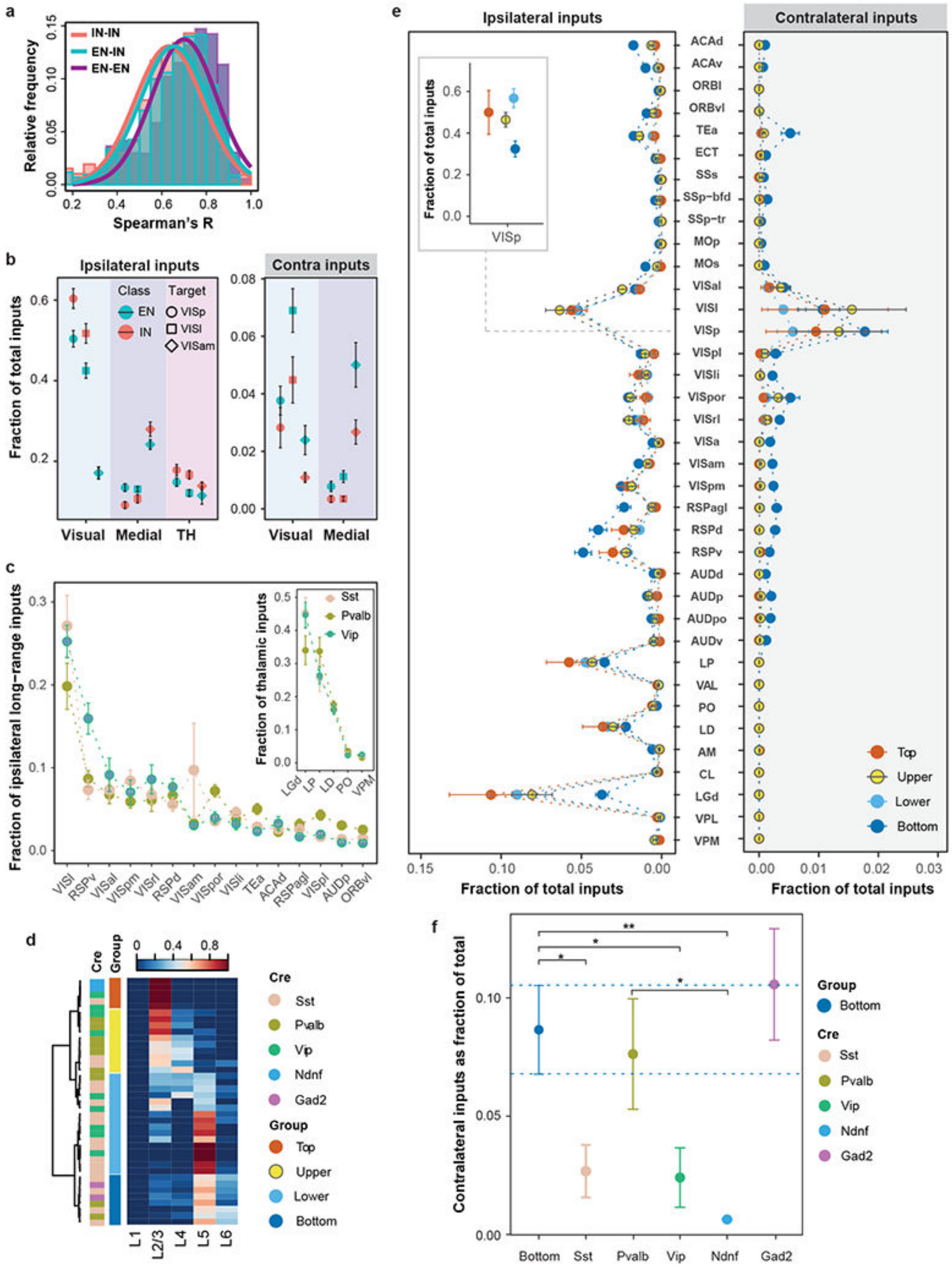

Figure 5. Comparison of brain-wide input patterns to different interneuron subclasses in the primary visual cortex.

(a) Frequency distribution of Spearman's R values for brain-wide input patterns to different excitatory neuron (EN) subclasses, those to different interneuron (IN) subclasses, and Rs measured between EN input patterns and IN input patterns. **(b)** Comparison of ipsilateral (left) and contralateral (right) inputs from the visual and medial cortical modules and thalamus to EN and IN cell classes located in the VISl (square), VISp (circle), and VISam (diamond). The numbers of EN experiments are 64 for VISp, 30 for VISl, and 14 for

VISam. The numbers of IN experiments are 39 for VISp, 26 for VISl, and 12 for VISam. Data are shown as mean ± s.e.m. **(c)** Comparison of ipsilateral cortical inputs and thalamic inputs to Sst (n=17), Pvalb (n=9) and Vip (n=9) cells in VISp. Data are shown as mean ± s.e.m. **(d)** Heatmap of starter cell layer distribution for the 39 interneuron experiments in VISp separating experiments into different depth groups. **(e)** Comparison of inputs from ipsilateral and contralateral cortical areas and thalamic nuclei to interneuron groups located in different depths of VISp. The numbers of independent experiments included are as follows: Top: n=5, Upper: n=10; Lower: n=16; Bottom: n=8. Data are shown as mean ± s.e.m. **(f)** Comparison of contralateral cortical inputs between the Bottom group and various interneuron subclasses. The numbers of independent experiments included are as follows: Bottom: n=8; Sst: n=17, Pvalb: n=9; Vip: n=9; Ndnf: n=2, Gad2: n=2. Data are shown as mean ± s.e.m. Independent two sample t test (two-sided), $^{**}p < 0.01$, $^{*}p < 0.05$, Bottom vs Sst: $p=0.018$, Bottom vs Vip: $p=0.017$, Bottom vs Ndnf: $p=0.0030$, and Pvalb vs Ndnf: $p=0.016$.

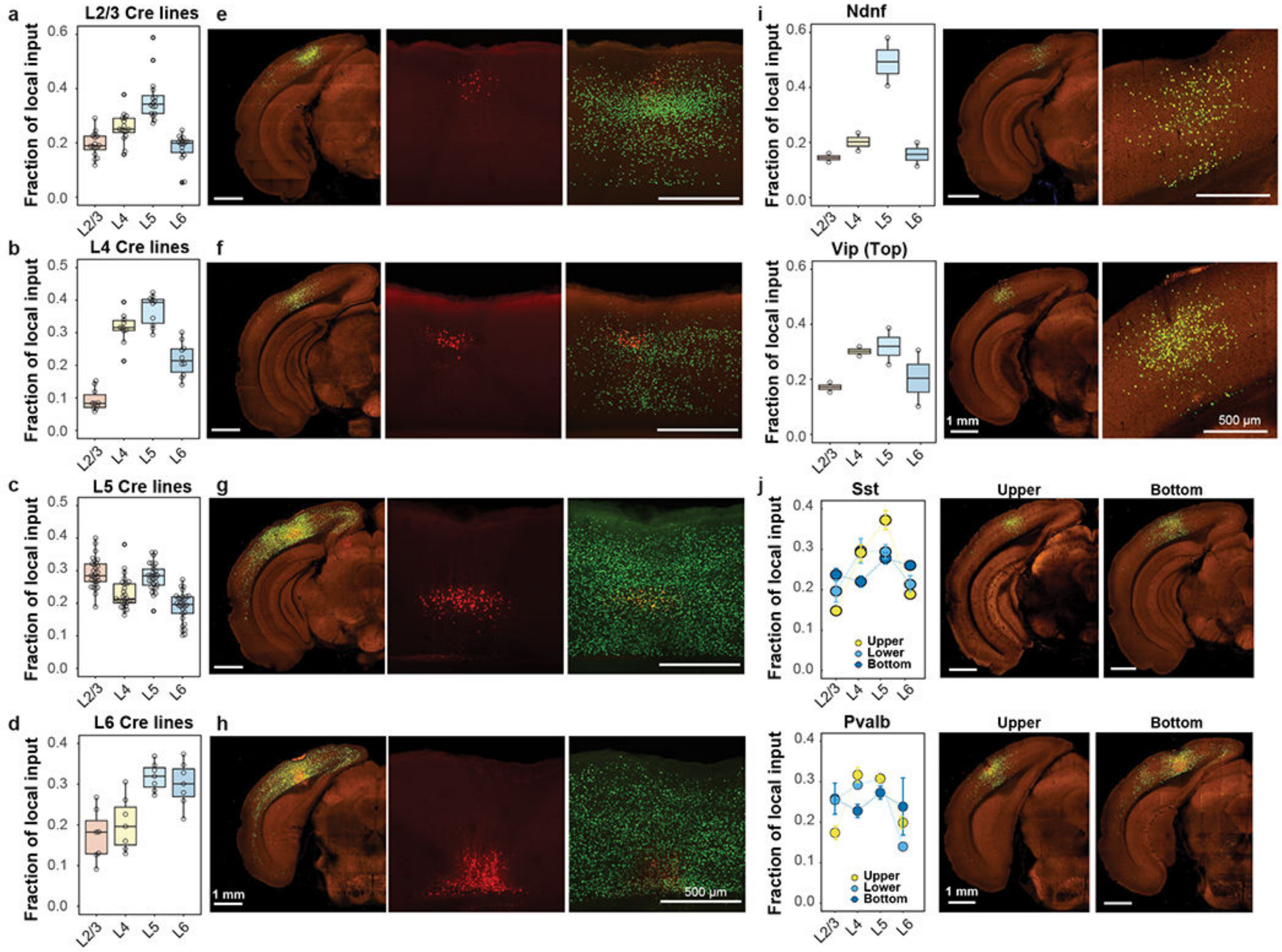

Figure 6. Comparison of local inputs to excitatory neurons and inhibitory interneurons in different depths of the primary visual cortex.

(a-d) Layer-specific inputs of ipsilateral VISp to excitatory neurons in L2/3 (a, n=16 independent experiments), L4 (b, n=10 independent experiments), L5 (c, n=29 independent experiments) and L6 (d, n=7 independent experiments) of VISp. **(e-h)** Representative images showing layer-specific local inputs to excitatory neurons in L2/3 (e), L4 (f), L5 (g) and L6 (h) of VISp. Left panels show STPT images of brain sections containing starter cells, and right two panels are confocal microscopic images showing the distribution of starter cells and local inputs. Starter cells are identified by the co-expression of dTomato from the AAV helper virus and nucleus-localized H2B-EGFP from the rabies virus. **(i)** Comparison of local input patterns to Ndnf-Cre and Vip-Cre experiments with Top distribution of starter cells (Ndnf and Vip: n=2 independent experiments). **(j)** Comparison of local inputs to Sst and Pvalb experiments with different depths of starter cell distribution. Representative images containing the injection sites are provided for Sst-Cre and Pvalb-Cre experiments in the Upper and Bottom groups. The numbers of independent Sst-Cre experiments in the Upper, Lower, and Bottom groups are 2, 10, and 4, respectively, and those of Pvalb experiments in the Upper, Lower, and Bottom groups are 6, 1, and 2, respectively. Data are shown as mean

± s.e.m. Box plots show median and interquartile range (IQR). Whiskers show the largest or smallest value no further than 1.5 × IQR from the hinge.

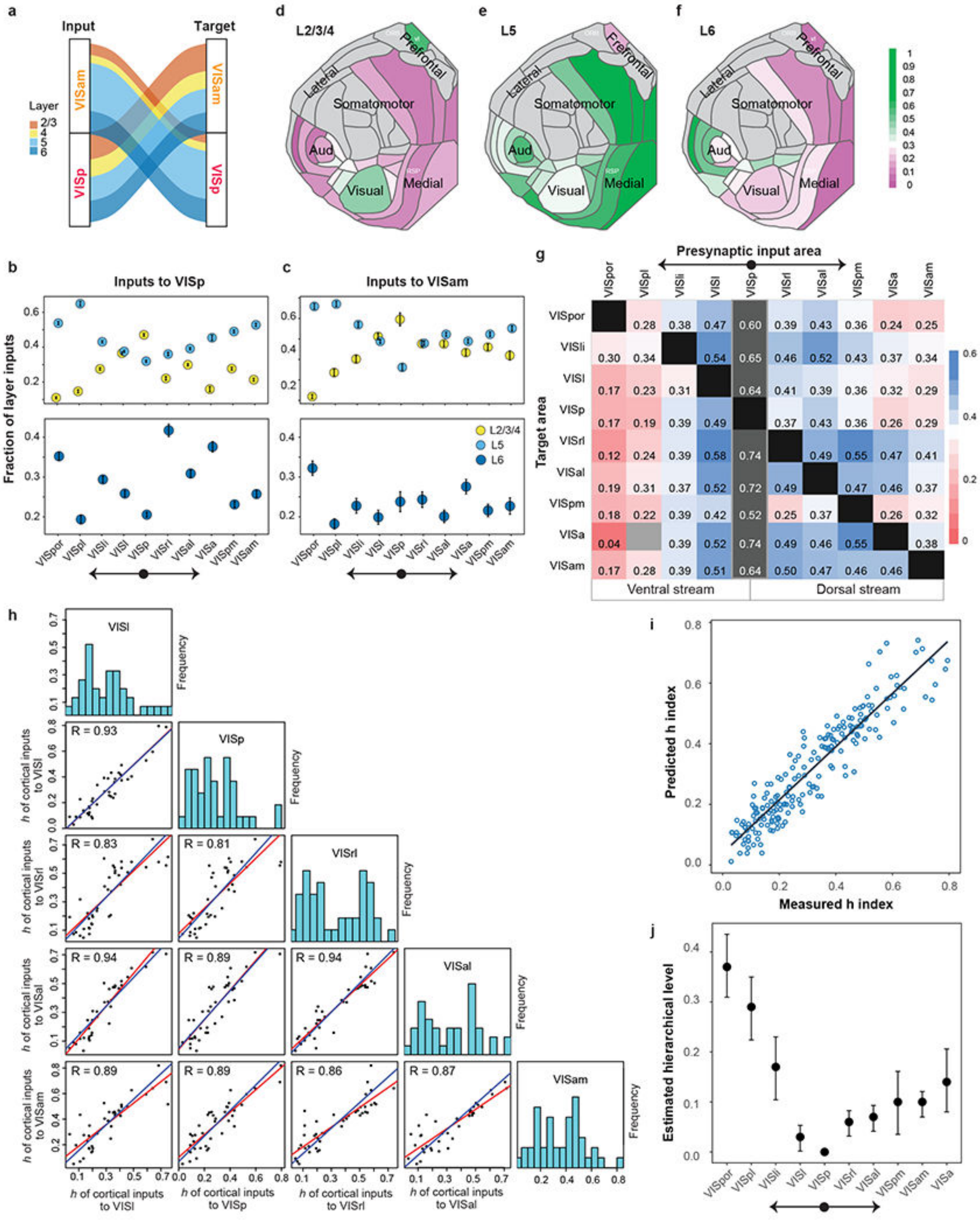

Figure 7. Relative hierarchical positions of the primary visual cortex and higher visual areas.

(a) Laminar distribution of inputs for connections between VISp and VISam. Mean fraction of layer-specific inputs between the source area and the target area was used. **(b-c)** Comparison of laminar distribution of visual area inputs to VISp (b, n=103 independent experiments) and VISam (c, n=26 independent experiments). Each dot represents the mean (± s.e.m.) fraction of layer-specific inputs. . Arrows indicate ascending order of hierarchical positions of the dorsal and ventral streams. **(d-f)** Comparison of the fraction of layer-specific inputs from various cortical areas (colored according to the mean fraction of inputs) to

VISp. **(g)** Matrix of *h* index of inputs from the 10 visual areas to the 9 targets. Each cell represents the mean *h* index of inputs in a given source area to a target area. Light gray denotes no availability of data. **(h)** Pairs plots showing the correlation of measured *h* index values of cortical source areas sending inputs to specific pairs of target areas. Each point represents the average pair of *h* index values obtained in a given source area to a pair of target areas. Red lines are the best fit lines (least-squares regression lines), and blue lines are the lines with a slope equal to 1 that best fit the points. **(i)** Correlation between measured and predicted *h* index values between cortical source areas and the five target visual areas in panel h. **(j)** Estimated hierarchical levels obtained by the linear regression model. The hierarchical level of VISp was set at zero. Error bars indicate 90% confidence intervals, with centrers representing the predicted hierarchical values for other visual areas. Visual areas are separated into the dorsal and ventral streams (to the right and left of VISp, respectively). Numbers of independent experiments: VISl: n=56, VISp: n=103, VISal: n=20, VISrl: n=23, and VISam: n=26.